ChemistrySelect

Research Article
doi.org/10.1002/slct.202302657

Chemistry Europe
European Chemical Societies Publishing

www.chemistryselect.org

DFT QM/MM MD Calculations to Identify Intermolecular Interactions within the Active Sites of $MraY_{AA}$ Bound to Antibiotics Capuramycin, Carbacaprazamycin, and 3′-Hydroxymureidomycin A

Elahe K. Astani[†],*[a, e] Saeid Malek Zadeh[†],[b, c, d] Soroush Sardari,[a] and Mahnaz Khosravian[e]

The bacterial transmembrane enzyme Phospho-*N*-acetylmuramoyl-pentapeptide translocase from *Aquifex aeolicus* ($MraY_{AA}$) plays an important role in the peptidoglycan biosynthesis of bacterial cell wall. The natural-product nucleoside inhibitors such as capuramycin, carbacaprazamycin, and 3′-hydroxymureidomycin A block the biosynthetic pathway of $MraY_{AA}$ by inhibiting its function. Since these $MraY_{AA}$ inhibitors have distinct complex chemical structures, the strengths of $MraY_{AA}$-inhibitor interactions strongly depend on the inhibitory structure. Here, the crystal structures of $MraY_{AA}$-capuramycin, $MraY_{AA}$-carbacaprazamycin, and $MraY_{AA}$-3′-hydroxymureidomycin A were separately optimized by quantum mechanics/molecular mechanics (QM/MM) approach in conjunction with molecular dynamics (MD) simulations. Further, quantum theory of atoms in molecules (QTAIM) and natural bond orbital (NBO) analyses at the M06-2X/6-31G** level were done on the active site of each optimized structure to specify the characteristics of intermolecular interactions of each cited inhibitor with the $MraY_{AA}$ active site residues. Our results revealed that Lys70, Thr75, Asp193, Asp196, Gly264, Asp265, and His325 play key roles in binding these inhibitors to $MraY_{AA}$ through hydrogen bonds of common types with strength ranging from van der Waals to covalent characters accompanying electrostatic and van der Waals interactions. $MraY_{AA}$-inhibitor interaction energies demonstrated that the $MraY_{AA}$ active site has the strongest intermolecular interactions with capuramycin.

Introduction

The peptidoglycan biosynthesis is a complex, multistep, and enzyme-catalyzed process that extensively occurs in the cytoplasm, on the inner side and the outer side of the cytoplasmic membrane of mycobacteria, Gram–positive and Gram–negative bacteria.[1–4] One of these key enzymatic reactions is the transfer of phospho-*N*-acetylmuramoyl-pentapeptide (P–MurNAc–pp) from the hydrophilic precursor uridine diphosphate-MurNAc-pentapeptide (UM5A) to the carrier lipid undecaprenyl phosphate (C_{55}–P) with the help of a Mg^{2+} cofactor and the production of undecaprenyl-pyrophosphoryl-MurNAc-pp, also known as lipid I, and uridine monophosphate (UMP).[5,6] This critical reaction is catalyzed by an integral transmembrane enzyme called phospho-*N*-acetylmuramoyl-pentapeptide translocase (MraY).[7] Structurally, MraY is well-known as a suitable bacterial protein drug target for five classes of the natural-product nucleoside antibiotics, including muraymycins, tunicamycins, capuramycins, caprazamycins, and mureidomycins.[8–10] Although peptidoglycan is a major constituent of the bacterial cell wall that protects the cell membrane and its contents,[4] the bacterial peptidoglycan biosynthetic pathway can be blocked and inhibited by binding these antibiotics to MraY.[11–14] Since each of these MraY inhibitors has an individual chemical structure with a shared uridine moiety,[10] all of them inhibit the MraY through a distinct inhibitory mechanism.[2,13,15,16]

Structurally, all five inhibitors have a common uridine moiety, including a uracil base and a ribose sugar (with two hydroxyl groups).[10] Among them, 3′-hydroxymureidomycin A (MUR) and muraymycin D2 (MD2) are also known as the uridyl-peptide antibiotics (UPAs) due to the presence of the peptidic residues attached to the uridine of MUR and MD2 via an enamide linker and an aminopropyl linker, respectively.[10,17,18] The *meta*-tyrosine and methionine are the peptidic residues of MUR (Figure 1a), while L-epicapreomycidine, L-valine, and L-leucine form the peptidic moiety of MD2 (Figure 1b). In each UPA, the cited peptidic residues are united together via a urea dipeptide motif. Similar to the MD2, the nucleoside portion of carbacaprazamycin (CAR) contains a 5-aminoribosyl moiety linked to its ribose sugar (Figure 1c).[10] Another common

[a] *Dr. E. K. Astani, Prof. Dr. S. Sardari*
Drug Design and Bioinformatics Unit, Medical Biotechnology Department, Biotechnology Research Center, Pasteur Institute of Iran, Tehran, 13169-43551, Iran
E-mail: Eastani@hotmail.com
Elahe.astani@modares.ac.ir

[b] *Dr. S. Malek Zadeh*
Genomics Research Center, Academia Sinica, Taipei, Taiwan 11529

[c] *Dr. S. Malek Zadeh*
Chemical Biology and Molecular Biophysics Program, Taiwan International Graduate Program, Academia Sinica, Taipei, Taiwan 11529

[d] *Dr. S. Malek Zadeh*
Institute of Bioinformatics and Structural Biology, National Tsing Hua University, Hsinchu, Taiwan 30013

[e] *Dr. E. K. Astani, Dr. M. Khosravian*
Department of Chemistry, Faculty of Science, Tarbiat Modares University, Tehran 14115-175, Iran

[†] *Deceased*

Supporting information for this article is available on the WWW under https://doi.org/10.1002/slct.202302657

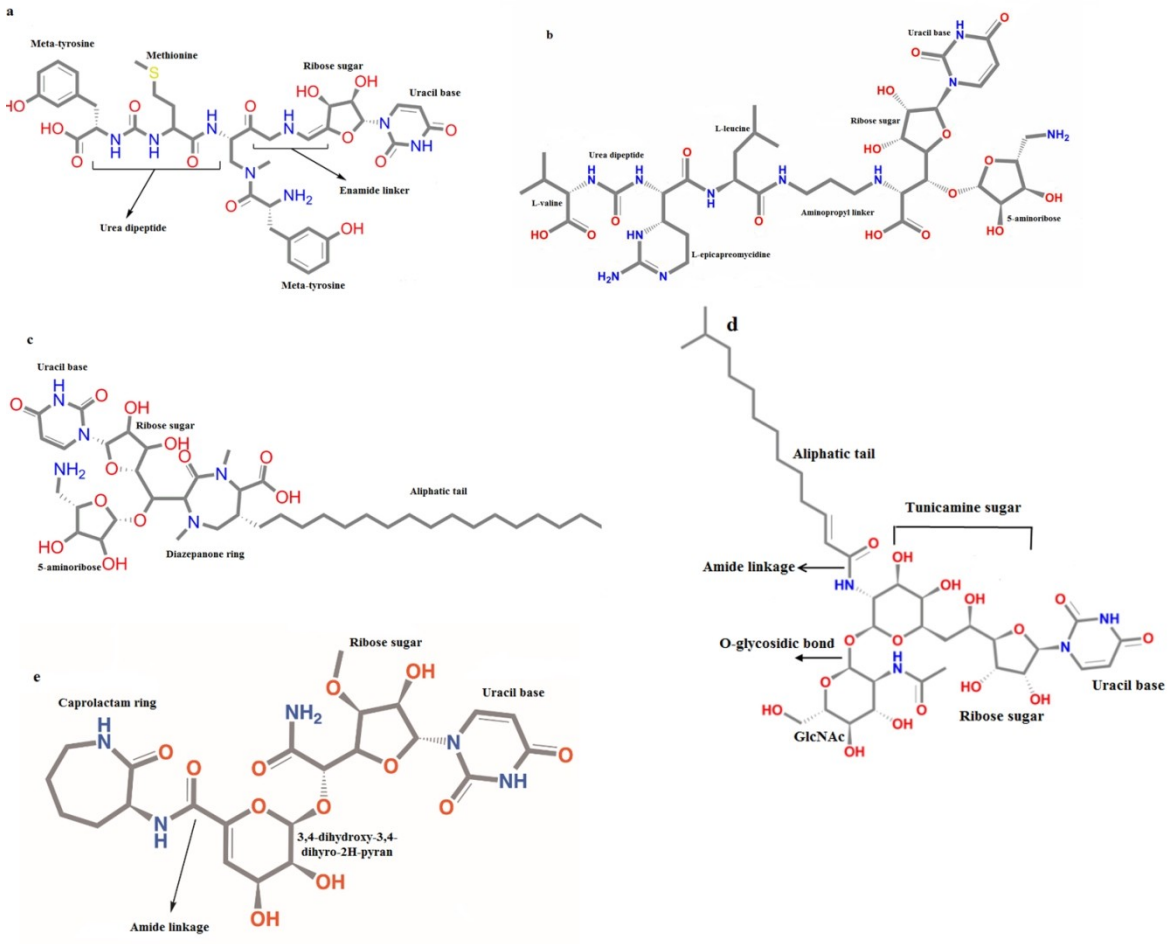

Figure 1. Chemical structures of (a) 3′-hydroxymureidomycin A, (b) muraymycin D2, (c) carbacaprazamycin, (d) tunicamycin, and (e) capuramycin nucleoside inhibitors.

structural scaffold of CAR with tunicamycin (TUN) is the presence of a single linear aliphatic chain in each of them. In the CAR, this aliphatic chain is a simplified saturated aliphatic tail attached to its diazepanone moiety (Figure 1c), while it is a monounsaturated aliphatic tail in the TUN that is bound to its tunicamine sugar moiety via an amide linkage. Tunicamine sugar is also linked to the *N*-acetylglucosamine (GlcNAc) moiety of TUN by an O-glycosidic bond (Figure 1d).[19–21] In addition to the uridine moiety, capuramycin (CAP) comprises the 3,4-dihydroxy-3,4-dihyro-2H-pyran and caprolactam (CPL) moieties that are attached together by an amide linkage (Figure 1e).[10]

To comprehend the inhibitory mechanism, the crystal structures of MraY bound to each of these aforementioned inhibitors have been solved by X-ray diffraction. The crystal structure of the apoMraY from thermophilic bacterium *Aquifex aeolicus* ($MraY_{AA}$) was the first released structure that is available in the Protein Data Bank (PDB) with PDB code 4J72.[22] The second crystal structure of $MraY_{AA}$ was obtained in complex with muraymycin D2 (PDB ID: 5CKR).[8] The third crystal structure of MraY from *Clostridium bolteae* ($MraY_{CB}$) bound to tunicamycin is accessible in the PDB with code 5JNQ.[9] Recently, three new structures of $MraY_{AA}$ have been released in the PDB under accession codes 6OYZ, 6OYH, and 6OZ6 pertaining to the complex structures of $MraY_{AA}$-capuramycin, $MraY_{AA}$-carbacaprazamycin, and $MraY_{AA}$-3′-hydroxymureidomycin A, respectively.[10] The X-ray crystal structures of apo$MraY_{AA}$, $MraY_{AA}$–MD2, and $MraY_{CB}$–TUN reveal that these proteins were crystallized in dimeric state in the asymmetric unit.[8,9,22] In contrast, three-dimensional structures of $MraY_{AA}$–CAP, $MraY_{AA}$–CAR, and $MraY_{AA}$–MUR are as the hetero-oligomers with nanobody from lama Glama in the asymmetric unit.[10] Crystal structures of all five MraY nucleoside inhibitors, as well as apo$MraY_{AA}$, indicate that the MraY structure consists of ten transmembrane (TM1–TM10) helices, an interfacial helix (IH), a periplasmic β hairpin (PB), and five cytoplasmic Loops (loops A–E). TM9 is split into two helical segments (TM9a and TM9b). The active site of MraY is constituted by absolutely conserved polar and charged amino acid residues situated in the inner–leaflet membrane regions of TM3, TM4, TM5, TM8, and TM9b as well as in cytoplasmic Loops B, C, D, and E.[8–10,22]

According to the crystal structures of $MraY_{AA}$–MD2, $MraY_{AA}$–CAP, $MraY_{AA}$–CAR, and $MraY_{AA}$–MUR,[8,10] the inhibitor binding pocket in $MraY_{AA}$ is composed of residues Lys70, Thr75, Asn190, Asp193, Gly194, Leu195, Asp196, Asn255, Phe262,

Gly264, Asp265, Ala321, and His325. The $MraY_{CB}$–TUN crystal structure[9] shows that the tunicamycin binding pocket is formed by residues Lys111, Asn172, Phe173, Asp175, Gly176, Asp178, Asn221, Phe228, Asp231, His290, and His291. In each MraY-inhibitor, these residues play important roles in binding the pertinent nucleoside inhibitor to the MraY active site in order to form tightly-bound MraY-inhibitor complex because they can interact with the different moieties of each inhibitor via a variety of electrostatic, van der Waals (vdW), and hydrogen-bonding (H-bonding) interactions (collectively referred to as noncovalent intermolecular interactions).[23] Theoretical studies to determine the nature and strength of the MraY-inhibitor interactions not only provide a basis for comprehending the MraY-inhibitor binding mechanism but they also can be extremely helpful in future to develop new potent MraY-targeted nucleoside antibiotics. Nowadays, the parallel progress of theoretical methods and the rapid increase in capabilities of modern computers allow the extensive use of the hybrid quantum mechanics/molecular mechanics (QM/MM) methods based on classical molecular dynamics (MD) simulations as a powerful computational tool to complement the experimental findings on the protein–ligand interactions.[24–30] In QM/MM approach, the protein–ligand structure is divided into two regions, QM and MM.[30] The active site residues accompanying ligand, which are explicitly treated with a quantum-mechanical Hamiltonian, are in the QM region, whereas the rest of the protein amino acids concomitant with the explicit solvent molecules, which are treated with a classical-mechanical Hamiltonian, are in the MM region.[31,32] Density functional theory (DFT) methods or *ab initio* molecular orbital theory techniques are usually applied on the QM region.[30,33] The MM region is approximated by empirical or MM force fields.[34,35]

To gain physical insight into the protein–ligand interactions at the atomic level, Bader's quantum theory of atoms in molecules (QTAIM)[36–38] and natural bond orbital (NBO)[39,40] analyses are well-known as two reliable theoretical tools to better understand the intermolecular interactions, especially the H-bonding interactions. In the previous computational studies, we have elucidated in detail the characteristics of $MraY_{AA}$–MD2 and $MraY_{CB}$–TUN interactions at the DFT level by using QTAIM and NBO analyses.[41,42] The objectives of the present work are summarized in five points. The first is to utilize the standard CHARMM36 force field[43] protocol for sketching $MraY_{AA}$–CAP, $MraY_{AA}$–CAR, and $MraY_{AA}$–MUR structures. The second is to apply DFT QM/MM MD simulations for optimizing the individual structures. The third is to use the QTAIM and NBO analyses for specifying the nature and strength of H-bonding interactions of capuramycin, carbacaprazamycin, and 3′-hydroxymureidomycin A with the $MraY_{AA}$ active site residues. The fourth is to compare the binding strengths of these inhibitors to the interested active site. The fifth and last is to answer to the important question: which inhibitor has the strongest intermolecular interactions with the $MraY_{AA}$ active site residues? On the basis of the computational analysis data, the quantitative ligand-target relationship should be able to understand the influence of binding factors on biological effectiveness, and with the established relationship, compounds can be constructed with improved and optimal biological profiles but free of unwanted side effects in the future.

Computational Details

The Setup of the MD Simulations on the $MraY_{AA}$-Inhibitors

Lee et al.[10] have solved the X-ray crystal structures of $MraY_{AA}$–CAP, $MraY_{AA}$–CAR, and $MraY_{AA}$–MUR at the atomic resolutions of 3.62 Å, 2.95 Å, and 3.70 Å, respectively. Due to very low X-ray resolutions of these structures, the side chains of some residues in each $MraY_{AA}$-inhibitor complex couldn't be detected into the pertinent electron density map. A visual inspection of the $MraY_{AA}$–CAP crystal structure[10] displays that the side chains of residues Tyr21, Ile22, Ser41, Asn46, Arg47, Lys50, Gln52, Arg53, Lys71, Asp96, Lys121, Lys131, Phe134, Leu195, Ile300, Gln305, Ile306, Ile307, Arg310, and Lys357 in its protomer A were not resolved in the electron density map. In the protomer A of $MraY_{AA}$–CAR complex,[10] residues Phe14, Phe16, Asn17, Lys20, Tyr21, Arg47, Gln52, Val69, Lys126, Lys131, Ile307, Tyr308, Arg310, Trp311, Lys315, and Arg320 lack the side chains. In the protomer A of $MraY_{AA}$–MUR complex,[10] residues Phe16, Asn17, Val18, Lys20, Tyr21, Ile22, Asn46, Arg47, Lys50, Gln52, Arg53, Leu54, Lys70, Lys71, Tyr72, Arg94, Lys121, Lys126, Lys131, Asp153, Asp155, Glu165, Val172, Tyr174, Leu175, Lys221, Arg310, Trp311, Lys315, Arg316, Leu317, Lys319, and Leu329 lack the side chains.

Starting from the atomic coordinates of low-resolution crystal structures of $MraY_{AA}$–CAP, $MraY_{AA}$–CAR, and $MraY_{AA}$–MUR,[10] each $MraY_{AA}$-inhibitor complex was prepared to run MD simulations in several steps. First, protomer A of each $MraY_{AA}$-inhibitor complex was separated from its other protomers because MD simulations were performed only on its protomer A (Figure 2). Second, the proper topology and parameter entries were constructed for complex structure of each aforementioned inhibitor by the existing protein, lipid, carbohydrate, and nucleic acid topologies/parameters available within the CHARMM36 force field.[43] In the Supporting Information, we explained in detail how to build topology and parameter entries of these inhibitors (Tables S1–S6). Third, the topology/parameter entries of each inhibitor were added to the protein topology/parameter files. Fourth, $MraY_{AA}$-inhibitor structures were sketched by the protein–inhibitor topology files and the QwikMD plugin[44] in VMD software.[45]

In all three structures, the missing coordinates of all hydrogen and non-hydrogen atoms in the $MraY_{AA}$ protein were recreated by the protein topology file and the VMD. Based on the protonation states of titratable residues in the $MraY_{AA}$-inhibitor structures determined experimentally,[10] in the simulated structures of $MraY_{AA}$-inhibitors, the side chains of all Asp and Glu residues were modeled as the deprotonated carboxylic groups, whereas the side chains of all Arg and Lys residues were modeled as the protonated guanidinum and amino groups, respectively. In the simulated structures of $MraY_{AA}$–CAP and $MraY_{AA}$–MUR, the protonation states of imidazole rings in residues His219, His325, and His326 were occurred at their Nε2 positions, while the protonation state of His324 was occurred at its Nδ1 position in both structures. In the simulated $MraY_{AA}$–CAR structure, residues His219, His324, His325, and His326 were modeled as Hsd219, Hsd324, Hse325, and Hse326, respectively. The N-terminal of the first residue of protein was protonated and the C-terminal of its last residue was deprotonated. Fifth, Each $MraY_{AA}$-inhibitor complex was solvated by placing it into a periodic rectangular box filled with a 12 Å layer of TIP3P water molecules.[46] The total charges of these explicitly solvated systems were neutralized by adding a reasonable number of sodium (Na^+) and

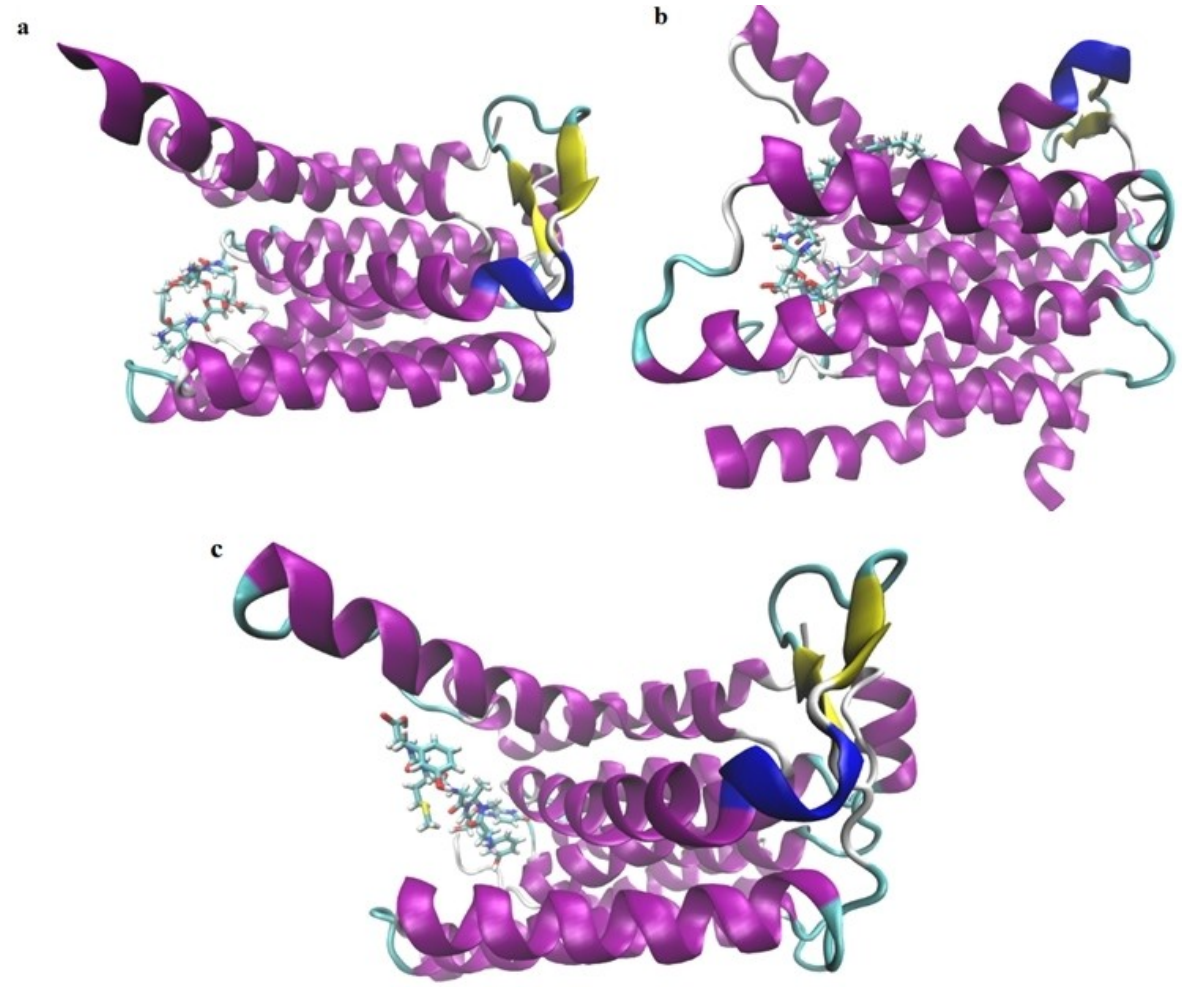

Figure 2. The three-dimensional structures of $MraY_{AA}$ protomer A bound to (a) capuramycin, (b) carbacaprazamycin, and (c) 3′-hydroxymureidomycin A.

chloride (Cl^-) ions to the protein surface. The exact numbers of ions added to the $MraY_{AA}$ surface in the solvated systems of $MraY_{AA}$–CAP, $MraY_{AA}$–CAR, and $MraY_{AA}$–MUR were 53 (23 Na^+ and 30 Cl^-), 58 (24 Na^+ and 34 Cl^-), and 62 (25 Na^+ and 37 Cl^-), respectively.

Sixth, minimization (for 200 ps), annealing (for 150 ps), equilibration (for 500 ps), and MD simulations were executed on each system under periodic boundary conditions by means of NAMD software.[47,48] MD simulations were initially run for 2 ns with a time step of 1 fs in the isobaric-isothermal (NPT) ensemble at constant pressure of 1 atm and temperature of 310 K. Afterwards, the simulations were continued in the canonical (NVT) ensemble between 10 and 20 ns at intervals of 1 fs. During the MD simulation of each $MraY_{AA}$-inhibitor complex, the whole solvated $MraY_{AA}$-inhibitor system, including all hydrogen and non-hydrogen atoms of $MraY_{AA}$ protein, inhibitor, and water molecules, was relaxed. A Langevin thermostat[49] was applied to control the temperature with a collision frequency of 1.0 ps^{-1}. Energies were stored every 1 ps and trajectory frames (atomic coordinates) were recorded every 5 ps. The long-range electrostatic interactions were treated by the particle mesh Ewald (PME) method,[50] while a cut-off distance of 12 Å was implemented to calculate the short-range van der Waals interactions with the Lennard–Jones potential. The distances of all covalent bonds involving hydrogen atoms were maintained by employing the SHAKE algorithm.[51]

The Setup of QM/MM Calculations on the Simulated $MraY_{AA}$-Inhibitor Structures

As depicted in Figure 1, capuramycin, carbacaprazamycin, and 3′-hydroxymureidomycin A share a common uridine moiety. In all $MraY_{AA}$-inhibitors,[10] the uridine moiety of each inhibitor is accommodated within the $MraY_{AA}$ uridine binding pocket. This pocket is composed of amino acid residues present in the Loops C and D, including Lys70, Gly194, Leu195, Asp196, Asn255, and Phe262 (Figure 3). There is a second binding pocket in $MraY_{AA}$ next to its uridine binding pocket called the uridine-adjacent pocket, which binds to 3,4-dihydroxy-3,4-dihyro-2H-pyran, 5-aminoribosyl, or *meta*-tyrosine moiety existing in capuramycin, carbacaprazamycin, and 3′-hydroxymureidomycin A, respectively.[10] This pocket is formed by residues Thr75, Asn190, Asp193, Gly264, and Asp265 (Figure 4). In the $MraY_{AA}$–CAP complex, the caprolactam binding pocket, consisting of Lys121, Leu122, and Lys125, is a unique binding site on the cytoplasmic face of $MraY_{AA}$, which accommodates the caprolactam moiety of capuramycin (Figure 5a). In the $MraY_{AA}$–MUR complex, Gln305 and Ala321 in the TM9b helix and His325 in the Loop E helix create a pocket for inserting the urea dipeptide motif of 3′-hydroxymureidomycin A (Figure 4c). In the $MraY_{AA}$–CAR complex, the TM9b/Loop E pocket binds to the diazepanone moiety of carbacaprazamycin, while its aliphatic tail is placed in a hydrophobic pocket formed by residues Ile130, Phe134,

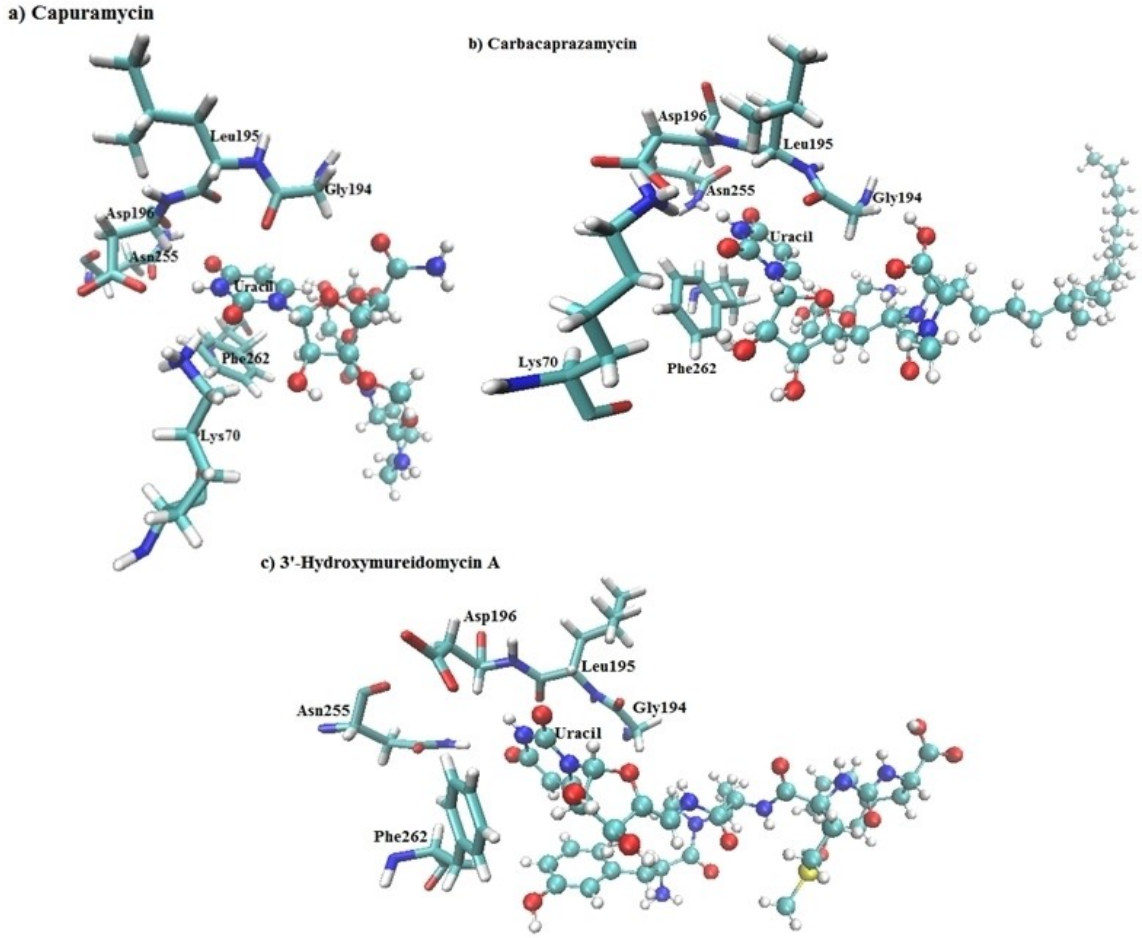

Figure 3. Residues Lys70, Gly194, Leu195, Asp196, Asn255, and Phe262 encompass the uridine moiety of (a) capuramycin, (b) carbacaprazamycin, and (c) 3′-hydroxymureidomycin A inside the $MraY_{AA}$ uridine binding pocket.[10] The active site residues are shown in licorice and each inhibitor is depicted in ball and sticks.

Phe180, Val183, Gly184, Ser185, Asn187, Leu191, Val296, Thr299, Val302, Ile303, and Ile306 (Figure 5b–c).

To set up the QM/MM calculations, the final frame of each $MraY_{AA}$-inhibitor simulated in the NVT ensemble was used to sketch the QM and MM regions by the QwikMD plugin[44] in VMD.[45] In each equilibrated structure, the inhibitor binding pocket, including the active site residues and the relevant inhibitor, was selected as the QM region, whereas the rest of the $MraY_{AA}$ residues along with TIP3P water molecules were considered as the MM region. Hence, three QM regions (QM models) were sketched. QM model I contains all of the atoms of capuramycin inhibitor and residues present in the capuramycin binding pocket in the equilibrated $MraY_{AA}$–CAP structure. QM model II includes all of the atoms of carbacaprazamycin inhibitor and residues present in the carbacaprazamycin binding pocket in the equilibrated $MraY_{AA}$–CAR structure. QM model III contains all of the atoms of 3′-hydroxymureidomycin A inhibitor and residues present in the 3′-hydroxymureidomycin A binding pocket in the equilibrated $MraY_{AA}$–MUR structure. Accordingly, QM models I, II, and III consist of 315, 582, and 373 QM atoms, respectively. These three QM models can be seen in Figures S1–S3 of the Supporting Information.

To run the QM/MM calculations, all QM atoms of each model were optimized by the hybrid meta-GGA density functional (M06-2X)[52–54] in conjunction with 6-31G** basis set. The MM regions were described by the CHARMM36 force field.[43] During the QM/MM calculations, the positions of the non-hydrogen atoms of each QM model were kept frozen. The QM/MM calculations were carried out with the integration time step of 0.5 fs in the NVT ensemble by using the NAMD/ORCA interface.[55–57] The Electrostatic interactions arising from the classical partial charges of MM atoms nearby all QM atoms were treated by an electrostatic embedding scheme.[58,59] The empty valences at the covalent bonds crossing the QM/MM boundary were filled by hydrogen link atoms with the Charge Shift (CS) treatment.[60,61]

Theoretical Tools Used on the QM Models to Identify the H-bonding Interactions of Individual Inhibitors with the $MraY_{AA}$ Active Site

QTAIM, primarily developed by Richard Bader et al.,[36–38] acts as a useful tool in analyzing the intramolecular and intermolecular interactions and classifying their strengths in terms of the electron density distribution function, ρ (r). The ρ (r) is a quantum-mechanical observable containing significant information from a molecular system that can be extracted from the corresponding many particle wave function ψ (x_1, x_2, …, x_N) as:[62]

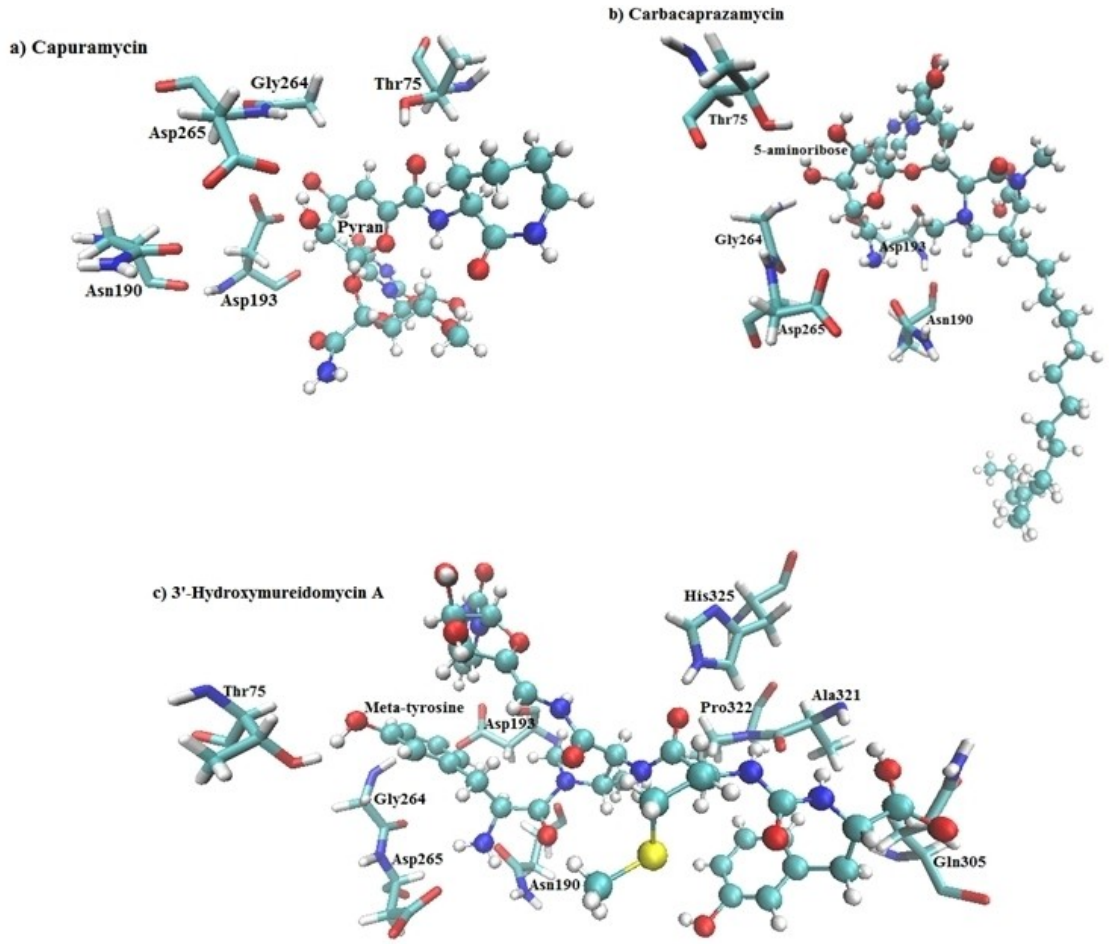

Figure 4. Residues Thr75, Asn190, Asp193, Gly264, and Asp265 enclose (a) the 3,4-dihydroxy-3,4-dihyro-2H-pyran in capuramycin, (b) the 5-aminoribose in carbacaprazamycin, and (c) he *meta*-tyrosine moiety in 3′-hydroxymureidomycin A inside the $MraY_{AA}$ uridine-adjacent pocket. Its urea dipeptide motif is surrounded by residues Gln305, Ala321, Pro322, and His325 in the TM9b/Loop E pocket.[10] The active site residues are shown in licorice and each inhibitor is depicted in ball and sticks.

$$\rho(r) = N\sum_{\sigma}\int |\psi(x_1, x_2, \ldots, x_N)|^2 d^3r_2 \ldots d^3r_N \tag{1}$$

A convenient quantitative method for analyzing the topology of ρ (r) is to consider the first derivative (gradient) of electron density, $\nabla\rho$(r). A point in space where the $\nabla\rho$ vanishes is called the critical point (CP):[62,63]

$$\nabla\rho = i\frac{d\rho}{dx} + j\frac{d\rho}{dy} + k\frac{d\rho}{dz} \rightarrow \left\{\begin{array}{l} = \vec{0}\ (\text{at critical points and at } \infty) \\ \textit{generally} \neq \vec{0}\ (\textit{at any other point}) \end{array}\right\} \tag{2}$$

A CP may be a saddle point, a local maximum, or a local minimum in the $\nabla\rho$ path. It is possible to recognize the various critical points by considering the second derivatives of the electron density. Mathematically, the second derivatives of ρ (r) at CP are represented by a 3×3 square matrix (a symmetric matrix) called Hessian matrix that is expressed in Cartesian coordinates as:[62,63]

$$A(r_c) = \begin{pmatrix} \frac{\partial^2\rho}{\partial x^2} & \frac{\partial^2\rho}{\partial x\partial y} & \frac{\partial^2\rho}{\partial x\partial z} \\ \frac{\partial^2\rho}{\partial y\partial x} & \frac{\partial^2\rho}{\partial y^2} & \frac{\partial^2\rho}{\partial y\partial z} \\ \frac{\partial^2\rho}{\partial z\partial x} & \frac{\partial^2\rho}{\partial z\partial y} & \frac{\partial^2\rho}{\partial z^2} \end{pmatrix}_{r'=r_c} \tag{3}$$

By rotating the coordinate system through the unitary transformation, the Hessian matrix is diagonalized:[63]

$$\Lambda(r_c) = \begin{pmatrix} \frac{\partial^2\rho}{\partial x'^2} & 0 & 0 \\ 0 & \frac{\partial^2\rho}{\partial y'^2} & 0 \\ 0 & 0 & \frac{\partial^2\rho}{\partial z'^2} \end{pmatrix}_{r'=r_c} = \begin{pmatrix} \lambda_1 & 0 & 0 \\ 0 & \lambda_2 & 0 \\ 0 & 0 & \lambda_3 \end{pmatrix} \tag{4}$$

where Λ (r_c) matrix is the diagonal form of Hessian matrix and the diagonal elements of λ_1, λ_2, and λ_3 are the eigenvalues of this matrix (or local curvatures of the ρ (r) at CP). λ_1 and λ_2 are the two negative perpendicular curvatures of the ρ (r) at the CP, whereas λ_3 is its positive parallel curvature at the CP.[62] The sum of these three eigenvalues (e.g., the trace of the diagonalized Hessian matrix) is known as the Laplacian of electron density, $\nabla^2\rho$ (r), which is written as:[62,63]

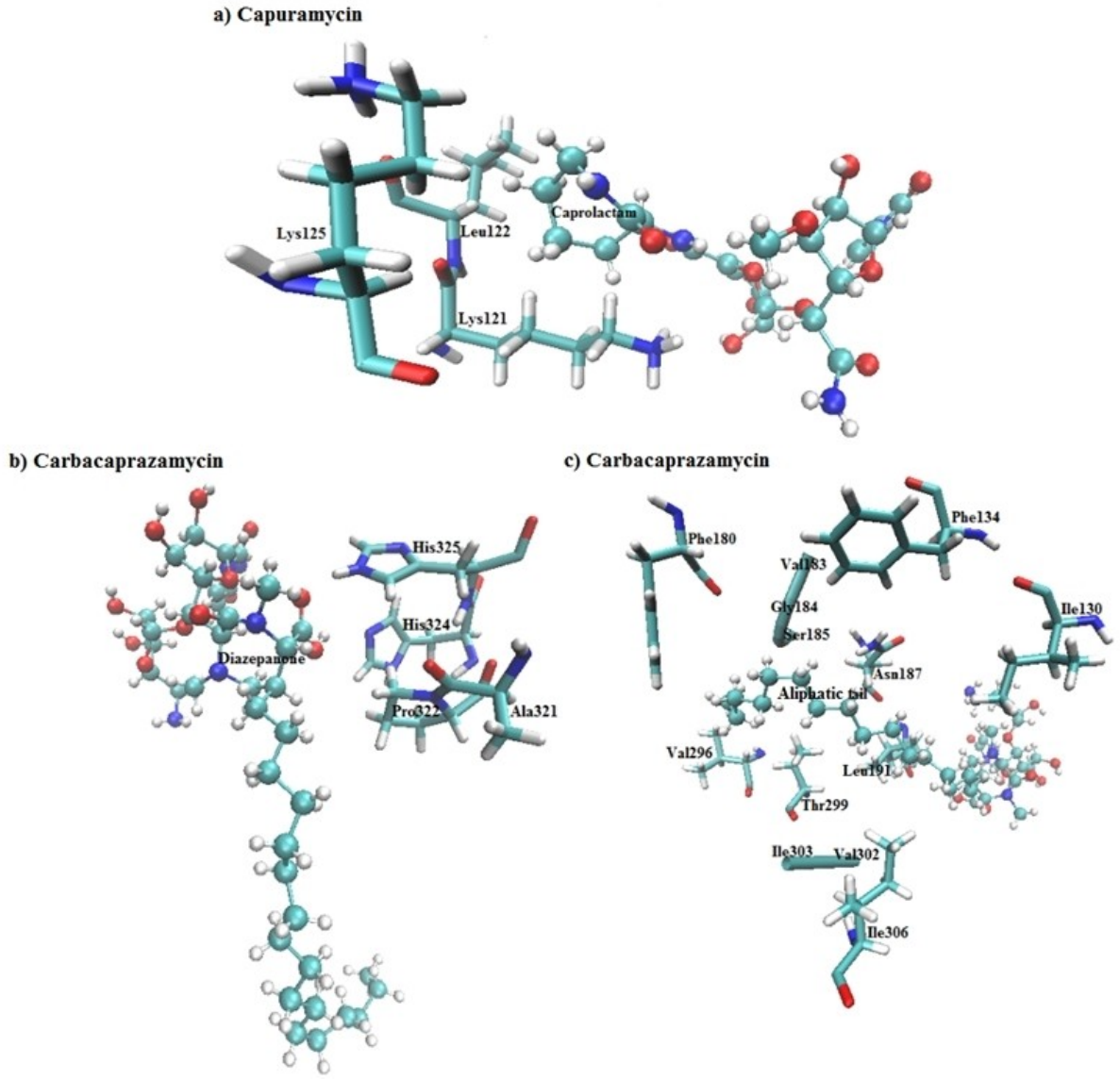

Figure 5. (a) The caprolactam moiety of capuramycin is located in the MraY$_{AA}$ caprolactam binding pocket by its residues Lys121, Leu122, and Lys125. (b) Residues Ala321, Pro322, His324, and His325 incorporate the diazepanone moiety of carbacaprazamycin into the MraY$_{AA}$ TM9b/Loop E pocket. (c) Its aliphatic tail binds to a hydrophobic pocket constituted by Ile130, Phe134, Phe180, Val183, Gly184, Ser185, Asn187, Leu191, Val296, Thr299, Val302, Ile303, and Ile306.[10] The active site residues are shown in licorice and each inhibitor is depicted in ball and sticks.

$$\nabla^2\rho(r) = \nabla.\nabla\rho(r) = \frac{\partial^2\rho(r)}{\partial x'^2} + \frac{\partial^2\rho(r)}{\partial y'^2} + \frac{\partial^2\rho(r)}{\partial z'^2} = \lambda_1 + \lambda_2 + \lambda_3 \quad (5)$$

Critical points are grouped into four classes based on their rank (the number of non-zero eigenvalues of the ρ (r) at CP) and signature (the sum of the signs of these eigenvalues) including the nuclear attractor (NA), the bond critical point (BCP), the ring critical point (RCP), and the cage critical point (CCP).[63] BCP is a saddle point that appears between two nuclei joining together by an atomic interaction line named the bond path (BP).[62] The $\nabla^2\rho$ (r) is a measure of local concentrations of ρ (r) with a negative or positive sign that has the order of ρ (r). The $\nabla^2\rho$ (r) at the BCP is related to the energetic topological parameters via the virial equation:[64,65]

$$\frac{1}{4}\nabla^2\rho_{BCP}(r) = 2G_{BCP}(r) + V_{BCP}(r) \quad (6)$$

$$H_{BCP}(r) = G_{BCP}(r) + V_{BCP}(r) \quad (7)$$

where G_{BCP} (r), V_{BCP} (r), and H_{BCP} (r), are the kinetic, potential, and total electronic energy densities at BCP, respectively. The G_{BCP} (r) is a positive quantity and the V_{BCP} (r) is a negative quantity. If the negative potential contribution at the BCP is dominant, the signs of $\nabla^2\rho_{BCP}$ and H_{BCP} are also negative, which indicates the charge concentration at this BCP and the presence of a shared interaction (covalent bond) at atom-atom region. In this case, ρ_{BCP} is greater than 0.20 atomic units (a. u.) and its $\nabla^2\rho_{BCP}$ is a large negative value. The positive sign of $\nabla^2\rho_{BCP}$ denotes the dominance contribution of positive kinetic due to the depletion of electron charge at BCP and the appearance of a closed-shell (such as vdW, ionic, H-bonding, etc.) interaction at this BCP. In this case, ρ_{BCP} is smaller than

0.10 a.u. and its $\nabla^2\rho_{BCP}$ is a low positive value.[62,63,66,67] Since the analysis of bond path and the associated properties of ρ_{BCP} (*r*), including $\nabla^2\rho_{BCP}$ (*r*), G_{BCP} (*r*), V_{BCP} (*r*), and H_{BCP} (*r*), provides valuable information on the nature of the interatomic interactions, QTAIM analysis was done on all three QM models at the M06-2X/6-31G** level by utilizing AIM 2000 program package.[68]

NBO analysis is another useful computational tool to describe a hydrogen bond (H-bond) in terms of the charge transfer (CT) interaction from the lone pair orbital of an electron donor (proton acceptor), n_B, into the valence antibonding orbital of an electron acceptor (proton donor), σ^*_{A-H}.[39,40,69] The energy of CT interaction, $n_B \rightarrow \sigma^*_{A-H}$, is called the second-order stabilization energy, $E^{(2)}$, and is calculated by the second-order perturbation theory as:[40]

$$E^{(2)} = \Delta E_{CT} = \Delta E(n_B \rightarrow \sigma^*_{A-H}) = -2\frac{\langle n_B|F|\sigma^*_{A-H}\rangle^2}{(\varepsilon(\sigma^*_{A-H}) - \varepsilon(n_B))} \quad (8)$$

where $\langle n_B|F|\sigma^*_{A-H}\rangle$and $\varepsilon(\sigma^*_{A-H}) - \varepsilon(n_B)$ are the Fock matrix element and energy difference between the donor and the acceptor orbitals, respectively. To evaluate the strengths of local orbital partners in the H-bonds, NBO analysis was carried out on all three QM models at the respective level by including the solvent effects using the polarizable continuum model (PCM) approach[70–72] and by employing ORCA program package.[56,57] It is worth noting that each of these QM models used for QTAIM and NBO analyses was based on the snapshot taken from the final frame of the pertinent $MraY_{AA}$-inhibitor optimized by QM/MM calculation.

Results and Discussion

In this study, the MD simulations were performed on $MraY_{AA}$–CAP, $MraY_{AA}$–CAR, and $MraY_{AA}$–MUR complex structures and then the active site of each simulated structure was modeled as a QM region. M06-2X functional in conjunction with 6-31G** basis set was applied for the geometry optimizations of the QM models. Afterwards, the QTAIM and NBO analyses were implemented on the optimized QM models to determine the nature and strength of the intermolecular interactions of each interested inhibitor with the $MraY_{AA}$ active site residues. In the following, the results extracted from these calculations are presented and discussed in separate sections.

MD Simulations of the MraY-Nucleoside Inhibitors

Since the MraY-inhibitor embedded in the explicit solvent is a dynamical system, the atomic coordinates both of the MraY residues and of the inhibitor were deviated from their primary atomic positions defined in the MraY-inhibitor crystal structure (as reference structure) over the simulation time. In other words, the atomic positions of the active site residues and the interested nucleoside inhibitor within the MraY inhibitor binding pocket in the simulated MraY-inhibitor structure were different from those in the MraY-inhibitor crystal structure. We thus employed the root mean square deviation, RMSD, as a numerical criterion to measure the differences between the atomic coordinates in the equilibrated structure and the reference structure which is obtained as below:[45]

$$RMSD(t) = \sqrt{\frac{\sum_{i=1}^{N_{atoms}} |r_i(t) - r_i(0)|^2}{N_{atoms}}} \quad (9)$$

where $r_i(0)$ represents the initial coordinate of atom *i* in the crystal structure and $r_i(t)$ is its final position at time *t* in the equilibrated structure. The amount of the RMSD variations of a given protein and subsequently its time required to reach the structural equilibrium depend on its initial atomic coordinates in the reference structure. In order to compute the RMSD values, the RMSD Trajectory Tool in VMD[45] included all atoms of each simulated MraY-inhibitor excluding its hydrogen atoms. The periods of MD simulations in the NVT ensemble for $MraY_{AA}$–CAP, $MraY_{AA}$–MD2, $MraY_{CB}$–TUN, $MraY_{AA}$–CAR, and $MraY_{AA}$–MUR structures were 10, 10, 15, 20, and 20 ns, respectively. The RMSD values of the simulated structures of all five MraY-inhibitors plotted versus the simulation times are shown in Figure 6. If the average RMSD, av.RMSD, of a simulated structure is in the range of 0.5–3 Å relative to its reference structure and standard deviation of its RMSD, sd.RMSD, is less than 1 Å, then, the simulated protein reaches the equilibrium state.[73–75] Our results affirm that the av.RMSDs and sd.RMSDs of these equilibrated structures are in the accepted rang (Table 1). It is worth pointing here that the simulations of $MraY_{AA}$–MD2 and $MraY_{CB}$–TUN structures have been performed previously.[41,42] To compare the simulation

Table 1. av.RMSDs, sd.RMSDs, and Average Electrostatic, van der Waals, and Nonbonded (Total) Interaction Energies of the Simulated Structures of MraY-Inhibitors Were Assessed During the Different Equilibrium Periods at 310 K in the NVT ensemble.

MraY-Inhibitors	av.RMSD (Å)	sd.RMSD (Å)	av.E_{Elec} (kJ/mol)	av.E_{vdW} (kJ/mol)	av.$E_{Nonbonded}$ (kJ/mol)
$MraY_{AA}$–MD2 [a]	1.55	0.16	−333.91	−249.00	−582.90
$MraY_{CB}$–TUN [b]	2.05	0.34	−360.69	−149.92	−510.61
$MraY_{AA}$–CAP	1.87	0.19	−452.86	−154.81	−607.67
$MraY_{AA}$–CAR	2.50	0.47	−254.95	−196.26	−451.20
$MraY_{AA}$–MUR	2.56	0.58	−195.43	−135.21	−330.64

[a] The av.RMSD, sd.RMSD, and av.energy components of the equilibrated structure of $MraY_{AA}$–MD2 are extracted from Ref. [41]. [b] The av.RMSD, sd.RMSD, and av.energy components of the equilibrated structure of $MraY_{CB}$–TUN are extracted from Ref. [42].

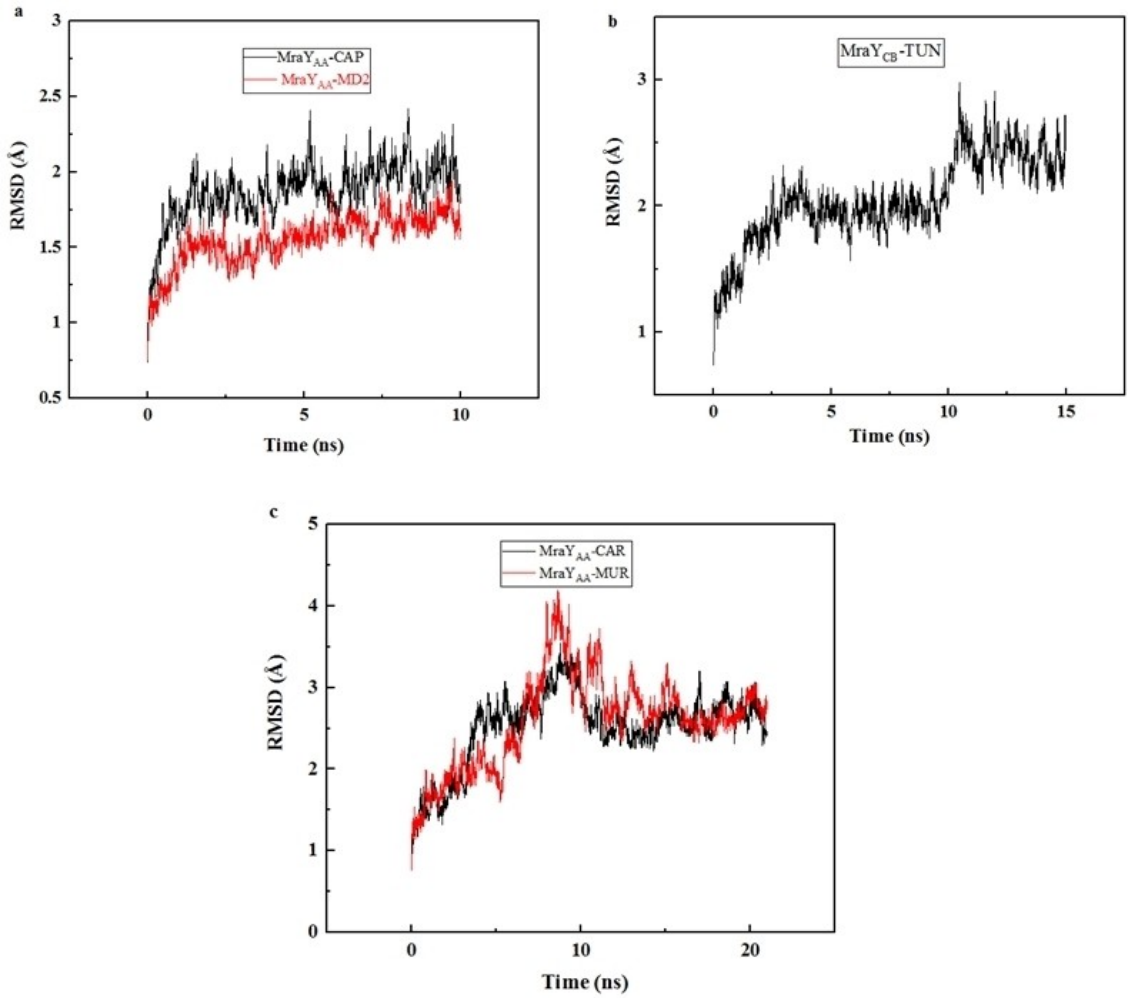

Figure 6. The RMSD values of the simulated structures of (a) MraY$_{AA}$–MD2[41] and MraY$_{AA}$–CAP, (b) MraY$_{CB}$–TUN,[42] (c) MraY$_{AA}$–CAR and MraY$_{AA}$–MUR are plotted against the simulation times. (In each case, benchmark is the whole MraY-inhibitor excluding its hydrogen atoms.)

results of these two structures with those of MraY$_{AA}$–CAP, MraY$_{AA}$–CAR, and MraY$_{AA}$–MUR structures, the simulation outcomes of MraY$_{AA}$–MD2 and MraY$_{CB}$–TUN structures are also mentioned in this section.

As mentioned above, the MraY-inhibitors are not static protein complexes in the explicit solvent. Hence, the atomic positions of each MraY-inhibitor repeatedly undergo dynamical rearrangements in the water box over the simulation time in order to search for a true local minimum in its dynamic energy landscape. Accordingly, the conformational rearrangements are continued until each simulated MraY-inhibitor reaches its true minimum. In this case, the simulated MraY-inhibitor achieves its equilibrated structure in the explicit solvent because it finds the conformation with the lowest-energy state in its energy landscape.[76] It is worth pointing that these MraY-inhibitors may undergo small or large conformational changes in the water boxes during the MD simulation. Among these simulated structures, MraY$_{AA}$–MD2 and MraY$_{AA}$–CAP have the shortest equilibrium time (10 ns) and the lowest av.RMSD values (Figure 6a and Table 1). Therefore, these two structures found their true local minima on the potential energy surface (PES) through small-scale dynamical rearrangements of their primary structures during the MD simulations. In contrast, great av.RMSD values of the equilibrated structures of MraY$_{CB}$–TUN, MraY$_{AA}$–CAR, and MraY$_{AA}$–MUR signify their large-scale conformational rearrangements in the water boxes (Table 1). Besides, they needed more times to achieve their equilibrium states (Figure 6b–c).

As mentioned earlier (Section 1), the nonbonded MraY-inhibitor interactions consist of electrostatic, vdW, and H-bonding interactions. As the potential energy function of CHARMM36 force field lacks an explicit potential function to calculate the H-bonding interaction energy,[34,43] the nonbonded interaction energies evaluated by MD simulations are the sum of the electrostatic and vdW interaction energies. The average electrostatic, van der Waals, and nonbonded (total) interaction energies, namely av.E_{Elec}, av.E_{vdW}, and av.$E_{Nonbonded}$, of the simulated structures of MraY-inhibitors are presented in Table 1. The graphical outputs of the nonbonded MraY-inhibitor interaction energies evaluated over the simulation times are displayed in Figures S4–S8 of the Supporting Information. MD simulation results indicate that the contributions of electrostatic

energies in all cases, especially in $MraY_{AA}$–CAP, are larger than those of vdW energies. Hence, the electrostatic interactions are mainly responsible for the stabilities of all five MraY-inhibitors. The binding strengths of the aforementioned inhibitors to the MraY active sites in terms of the average total interaction energies decrease as follows: capuramycin > muraymycin D2 > tunicamycin > carbacaprazamycin > 3′-hydroxymureidomycin A. Based on MD simulation results, the MraY active site has thus the strongest intermolecular interactions with capuramycin.

QM/MM Calculations on the Simulated $MraY_{AA}$-Inhibitor Structures

As mentioned earlier (Section 2), because of very low atomic resolutions of these three $MraY_{AA}$-inhibitors,[10] the side chains of some residues in each $MraY_{AA}$-inhibitor complex were not resolved in its electron density map. By performing DFT QM/MM MD simulations on these structures, not only the missing side chains of these residues were reconstructed but also their atomic coordinates were placed in the reasonable positions in these residues. By optimizing all three QM models at the DFT level, the coordinates of all their hydrogen and non-hydrogen atoms were accurately determined to characterize the conventional and unconventional H-bonds and CT interactions providing the binding of each cited inhibitor to the $MraY_{AA}$ active site. In the following, the importance and contribution of the H-bonding and CT interactions to the total intermolecular interactions of each inhibitor with the active site residues are defined by the QTAIM and NBO analyses.

Exploration of H-Bonding Interactions of Inhibitor–Residue Pairs in the QM Models I, II, and III by the QTAIM Analysis

The structural and topological parameters extracted from the geometry optimizations and the QTAIM analyses of all three QM models are tabulated in Table 2. It is worth pointing here that the ρ and $\nabla^2\rho$ values at the different hydrogen-bond critical points (HBCPs) detected in these three models are within the Koch–Popelier range.[77] To evaluate the H-bonding interaction strength, we calculated the H-bonding interaction energy (E_{HB}) of each H-bond by applying the relationship between V_{BCP} and E_{HB} established by Espinosa et al.[78–80] The absolute values of the assessed H-bond energies, $|E_{HB}|$, are available in Table 2. On the basis of $|E_{HB}|$ magnitude, the H-bonding interaction strength is classified as weak (4.18–16.74 kJ/mol), moderate (16.74–62.76 kJ/mol), or strong (62.76–167.36 kJ/mol) H-bond.[81–86]

As displayed in Figure 3, the uridine binding pocket in $MraY_{AA}$ is lined by Lys70, Gly194, Leu195, Asp196, Asn255, and Phe262. The QTAIM analysis identifies that the carbonyl oxygens of uracil base of both CAP and CAR form H-bonds of N–H···O and C–H···O types with Lys70 and Asp196 (Figure 7a–b). Large amounts of ρ_{BCP} (0.0633 a.u.), $\nabla^2\rho_{BCP}$ (0.1789 a.u.), and $|E_{HB}|$ (77.87 kJ/mol) on Hζ3···O39 BCP in the CAP–Lys70 pair demonstrate that the Nζ–Hζ3···O39 is a strong H-bond with an essentially covalent nature.[87] Indeed, it with an angle of 158.52° and a length of 1.54 Å is the strongest H-bond of capuramycin in the QM model I because it has the highest values of ρ_{BCP}, $\nabla^2\rho_{BCP}$, and $|E_{HB}|$ compared to the other H-bonds of CAP (Table 2). Due to increase in O52···Nζ distance, the strength of Nζ–Hζ2···O52 in the CAR–Lys70 pair is remarkably decreased and it is converted to a moderate H-bond with an $|E_{HB}|$ of 19.72 kJ/mol and a length of 2.13 Å in the QM model II. This H-bond is even weaker than moderate H-bond of Nζ–Hζ2···O33 ($|E_{HB}| = 36.72$ kJ/mol) in the MD2–Lys70 pair.[41] The uracil base of CAR also interacts with Lys70 through weak unconventional H-bond of Cδ–Hδ1···O52 (Figure 7b). Since the $|E_{HB}|$ (28.92 kJ/mol) of Cα–Hα···O36 in the CAP–Asp196 pair is larger than that (10.38 kJ/mol) of Cα–Hα···O56 in the CAR–Asp196 pair, the former H-bond is stronger than the latter H-bond. Besides, the CAR uracil base forms an additional H-bond (Nδ2–Hδ21···O56) with Asn255 (Figure 7b). Although this H-bond is not observed either in QM model I or in QM model III, such H-bond has been found between muraymycin D2 and Asn255 (Nδ2–Hδ22···O32)[41] as well as between tunicamycin and Asn221 in $MraY_{CB}$ (Nδ2–Hδ21···O28).[42]

As displayed in Figure 7a–c, H-bond of N–H···O type exists between Asp196 side chain carboxylate oxygen and the uracil base amide nitrogen of each inhibitor. As the largest values of ρ_{BCP} (0.0468 a.u.), $\nabla^2\rho_{BCP}$ (0.1568 a.u.), and $|E_{HB}|$ (50.69 kJ/mol) in the QM model III are assigned to N58–H581···Oδ1 in the MUR–Asp196 pair, this moderate interaction with a length of 1.64 Å and an angle of 173.04° is the strongest H-bond of MUR. Because the topological and geometrical parameters of N37–H371···Oδ1 in the CAP–Asp196 pair are approximately equal to those of N51–H511···Oδ1 in the CAR–Asp196 pair, the strengths of these two H-bonds in QM models I and II are almost the same (Table 2). It is worth stressing that Asp196 has the strongest H-bond with the uracil base of muraymycin D2 because N30–H301···Oδ1 in the MD2–Asp196 pair is a strong H-bond with an $|E_{HB}|$ of 177.72 kJ/mol.[41] The ribose sugar of CAP participates in two weak H-bonds of Cε–Hε1···O40 and Cα–Hα2···O10 with Lys70 and Gly194, respectively (Figure 7a). Weak Cα-Hα2···O47 H-bond is also seen in the CAR–Gly194 pair (Figure 7b). In addition to H-bonds, the uridine binding pocket in $MraY_{AA}$ is stabilized by the electrostatic interaction of the π···π stacking type that appears between Phe262 aromatic ring and the uracil base ring of CAP, CAR, MUR, or MD2[8,10,41] (Figure 7). The TUN uracil moiety also interacts with either Phe228 (in $MraY_{CB}$)[9,42] or Phe249 (in DPAGT1)[42,88] through the π···π stacking interaction.

The uridine-adjacent pocket in $MraY_{AA}$ is lined by residues Thr75, Asn190, Asp193, Gly264, and Asp265, which is occupied by the 3,4-dihydroxy-3,4-dihyro-2H-pyran in CAP (Figure 4a), 5-aminoribose in CAR (Figure 4b), or *meta*-tyrosine moiety in MUR (Figure 4c). The QTAIM analysis recognizes proton-donor (H-donor) role of Thr75 side chain hydroxyl oxygen in the formation of a moderate H-bond of Oγ1–Hγ1···O20 with the carbonyl oxygen of 3,4-dihydroxy-3,4-dihyro-2H-pyran moiety (Figure 8a). On the contrary, this oxygen acts as a proton-acceptor (H-acceptor) in the interactions of O14–H141···Oγ1, O12–H121···Oγ1, and O41–H411···Oγ1 with the hydroxyl groups of 5-aminoribosyl and *meta*-tyrosine moieties (Figure 8b–c). Of

Table 2. The Geometrical and Topological Parameters of the Electron Density in Various H···O and H···N BCPs Related to CAP-Residue, CAR-Residue, and MUR-Residue Pairs of QM Models I, II, and III Were Computed at the M06-2X/6-31G** Level.[a]

Proton donor	Proton acceptor	H-Bond	d	∠	ρ_{BCP}	$\nabla^2\rho_{BCP}$	H_{BCP}	$\lvert E_{HB}\rvert$
Lys70	CAP	Cε–Hε1···O40	2.39	165.37	0.0109	0.0340	−0.0079	10.60
Lys70	CAP	Nζ–Hζ3···O39	1.54	158.52	0.0633	0.1789	−0.0666	77.87
Lys70	CAR	Cδ–Hδ1···O52	2.40	125.61	0.0121	0.0408	−0.0082	11.66
Lys70	CAR	Nζ–Hζ2···O52	2.13	133.90	0.0185	0.0567	−0.0154	19.72
Thr75	CAP	Oγ1–Hγ1···O20	1.90	162.47	0.0257	0.0859	−0.0210	27.74
Thr75	CAP	Cγ2–Hγ23···O20	2.61	118.59	0.0084	0.0300	−0.0046	7.34
Lys121	CAP	Cε–Hε1···O29	2.53	145.95	0.0095	0.0311	−0.0058	8.48
Gly194	CAP	Cα–Hα2···O10	2.30	137.25	0.0131	0.0449	−0.0093	13.01
Gly194	CAR	Cα-Hα2···O47	2.55	142.08	0.0084	0.0292	−0.0053	7.79
Asp196	CAP	Cα–Hα···O36	1.99	144.80	0.0266	0.0829	−0.0227	28.92
Asp196	CAR	Cα–Hα···O56	2.43	156.44	0.0112	0.0333	−0.0077	10.38
Asn255	CAR	Nδ2–Hδ21···O56	2.21	146.46	0.0139	0.0447	−0.0111	14.63
Phe262	CAR	Cβ–Hβ1···O14	2.55	132.28	0.0083	0.0286	−0.0048	7.36
Gly264	CAP	N–H···O30	1.88	145.57	0.0309	0.1073	−0.0277	35.97
Gly264	CAP	Cα–Hα2···O31	2.69	147.77	0.0063	0.0225	−0.0033	5.31
Gly264	CAR	N–H···O12	1.95	116.24	0.0282	0.1164	−0.0247	34.38
Gly264	CAR	Cα-Hα2···O12	2.30	111.67	0.0166	0.0599	−0.0124	17.36
Ser268	CAR	Oγ–Hγ···N16	2.70	160.66	0.0067	0.0202	−0.0035	5.28
Ala321	MUR	N–H···O20	2.29	172.66	0.0107	0.0396	−0.0078	11.16
His325	CAR	Nε2–Hε2···O42	1.54	151.67	0.0629	0.2286	−0.0679	84.46
His325	MUR	Nε2–Hε2···O23	1.91	159.24	0.0244	0.0848	−0.0192	26.06
CAR	Thr75	O14–H141···Oγ1	1.94	131.12	0.0260	0.0891	−0.0240	30.76
CAR	Thr75	O12–H121···Oγ1	2.32	124.31	0.0124	0.0480	−0.0095	13.55
MUR	Thr75	O41–H411···Oγ1	2.05	129.04	0.0214	0.0725	−0.0193	24.78
CAR	Asn187	C31–H312···Nδ2	2.60	168.78	0.0096	0.0295	−0.0048	7.41
CAR	Asn190	N16–H1···O	2.48	165.09	0.0089	0.0293	−0.0059	8.40
CAR	Asn190	C20–H202···O	2.48	142.88	0.0092	0.0308	−0.0058	8.45
MUR	Asn190	C27–H272···O	2.37	145.59	0.0109	0.0372	−0.0076	10.68
MUR	Asn190	N33–H332···Oδ1	2.29	128.04	0.0135	0.0471	−0.0102	14.09
CAP	Asp193	C34–H341···Oδ1	2.45	157.26	0.0090	0.0296	−0.0060	8.47
CAP	Asp193	O30–H301···Oδ1	1.66	173.18	0.0497	0.1343	−0.0432	52.50
CAP	Asp193	O31–H311···Oδ2	1.71	160.47	0.0435	0.1087	−0.0340	41.69
CAR	Asp193	O12–H121···Oδ2	1.92	155.83	0.0272	0.0811	−0.0228	28.86
CAR	Asp193	O14–H141···Oδ2	2.21	147.57	0.0143	0.0455	−0.0120	15.44
CAR	Asp193	C13–H131···Oδ2	2.69	105.03	0.0086	0.0319	−0.0047	7.58
MUR	Asp193	C39–H391···Oδ2	1.97	172.31	0.0266	0.0744	−0.0225	27.79
CAP	Asp196	N37–H371···Oδ1	1.81	176.31	0.0335	0.0925	−0.0243	31.37
CAR	Asp196	N51–H511···Oδ1	1.82	161.05	0.0335	0.0968	−0.0256	33.03
MUR	Asp196	N58–H581···Oδ1	1.64	173.04	0.0468	0.1568	−0.0383	50.69
CAP	Asp265	O31–H311···Oδ1	2.32	111.06	0.0128	0.0486	−0.0101	14.13
CAR	Asp265	N16–H161···Oδ1	2.13	147.66	0.0198	0.0552	−0.0172	21.12
CAR	Asp265	N16–H1···Oδ2	2.51	112.54	0.0104	0.0394	−0.0068	10.23
MUR	Asp265	N33–H332···Oδ1	2.41	137.40	0.0096	0.0336	−0.0067	9.55
MUR	Ala321	N09–H091···O	2.40	160.50	0.0094	0.0319	−0.0066	9.28
MUR	Ala321	C17–H171···O	2.65	122.54	0.0071	0.0261	−0.0036	6.04

[a] The H-bond length (d) is in Angstrom (Å) and the H-bond angle (∠) is in degrees (°). All ρ_{BCP}, $\nabla^2\rho_{BCP}$, and H_{BCP} parameters are in atomic units (a.u.). $\lvert E_{HB}\rvert$ is in kJ/mol.

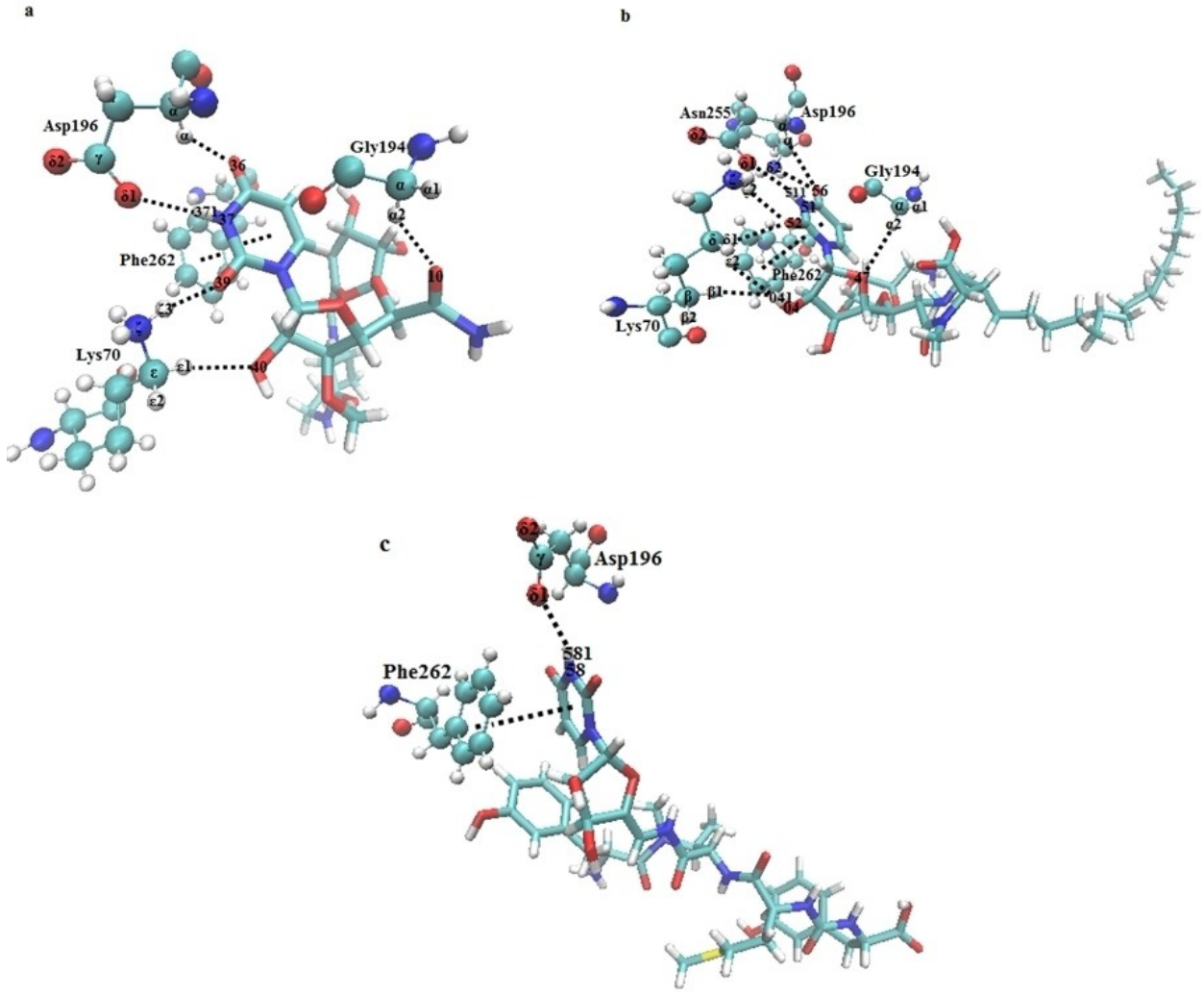

Figure 7. Residues Lys70, Gly194, Asp196, Asn255, and Phe262 provide the uridine moiety binding of (a) CAP, (b) CAR, and (c) MUR to the uridine binding pocket via H-bonds and the π···π stacking interactions. Residues are shown in ball and sticks and each inhibitor is depicted in licorice.

these, the largest amounts of ρ_{BCP} (0.0260 a.u.), $\nabla^2\rho_{BCP}$ (0.0891 a.u.), and $|E_{HB}|$ (30.76 kJ/mol) belong to the O14–H141···Oγ1 H-bond in the CAR–Thr75 pair (Table 2). It is thus the strongest among these four H-bonds. Additionally, weak H-bond of Cγ2–Hγ23···O20 is identified in the CAP–Thr75 pair (Figure 8a). Although, the 5-aminoribosyl moiety of MD2 is involved in a moderate H-bond (O24–H241···Oγ1) with Thr75,[41] TUN is unable to form such H-bond with the corresponding residue in $MraY_{CB}$ (Thr52).[42]

The hydroxyl oxygens of 3,4-dihydroxy-3,4-dihyro-2H-pyran moiety simultaneously play the H-donor and H-acceptor roles in the formation of the hydrogen bonds with Asp193 and Gly264. Analogously, the hydroxyl groups of 5-aminoribosyl moiety exhibit a similar manner in the interactions with Asp193 and Gly264. Therefore, H-bonds of N–H···O, O–H···O, and C–H···O kinds are formed between each of these residues and either CAP or CAR (Figure 8a–b). As seen in Table 2, N–H···O30 in the CAP–Gly264 pair is almost geometrically and topologically equivalent to N–H···O12 in the CAR–Gly264 pair. Because $|E_{HB}|$ (5.31 kJ/mol) of Cα–Hα2···O31 in the former pair is smaller than that (17.36 kJ/mol) of Cα-Hα2···O12 in the latter pair, Gly264 has a stronger unconventional H-bond with CAR than with CAP. It is worth pointing here that N–H···O23 in the MD2–Gly264 pair is a strong hydrogen bond ($|E_{HB}| = 92.26$ kJ/mol)[41] and there is no hydrogen bond between TUN and the corresponding residue in $MraY_{CB}$ (Gly230).[42] Asp193 carboxylate oxygens engage in the formation of C34–H341···Oδ1, O30–H301···Oδ1, and O31–H311···Oδ2 H-bonds with CAP as well as O12–H121···Oδ2, O14–H141···Oδ2, and C13–H131···Oδ2 H-bonds with CAR (Figure 8a–b). Since the BCP properties of these interactions are indicative of the presence of stronger H-bonds in the CAP–Asp193 pair (Table 2), the binding stability of 3,4-dihydroxy-3,4-dihyro-2H-pyran to Asp193 is greater than that of the 5-aminoribose to Asp193. In the MUR–Asp193 pair, the QTAIM analysis finds only C39–H391···Oδ2 H-bond with an $|E_{HB}|$ of 27.79 kJ/mol and a length of 1.97 Å (Figure 8c).

The amide nitrogen of 5-aminoribose acts as a H-donor for both Asp265 side chain carboxylate oxygens and Asn190

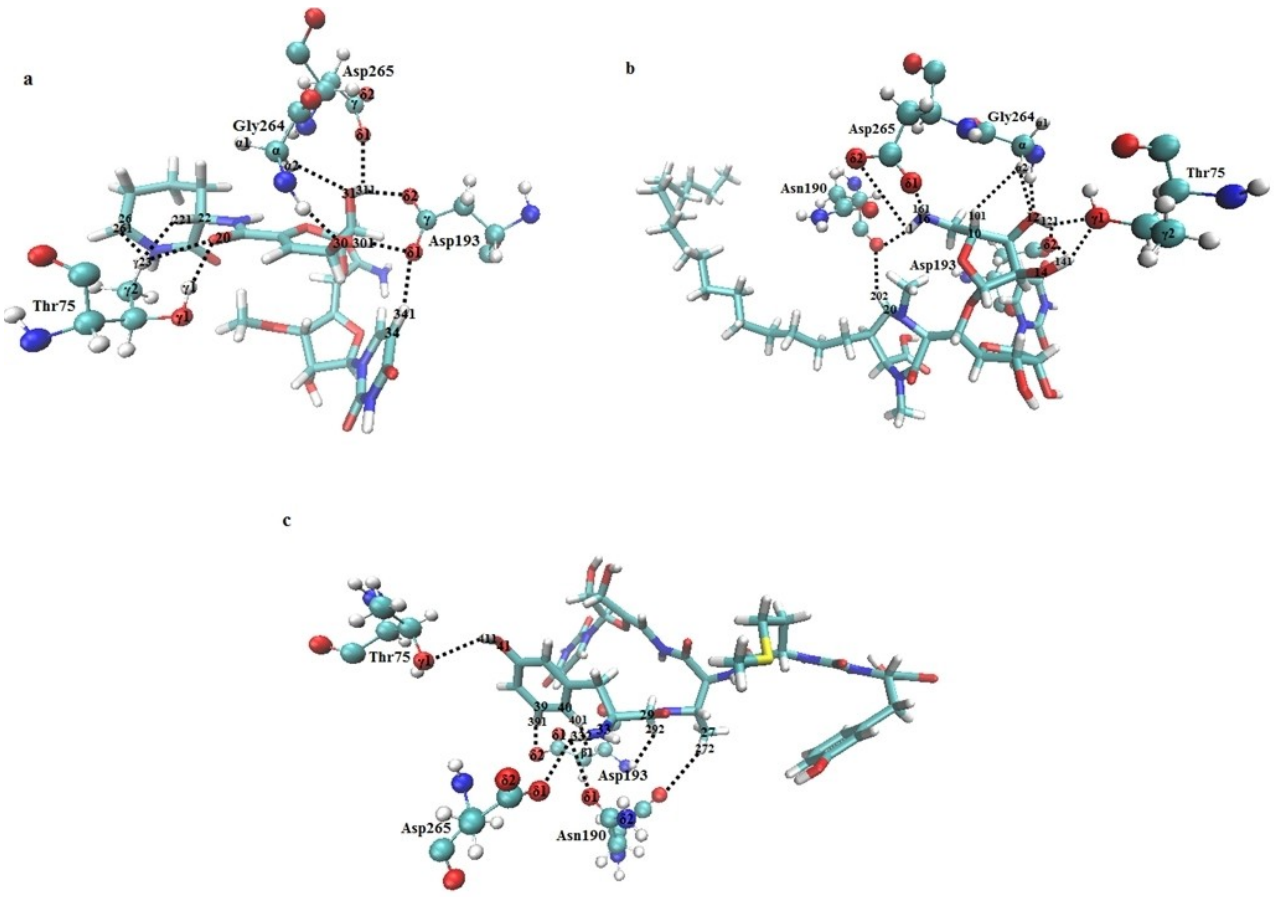

Figure 8. (a) The 3,4-dihydroxy-3,4-dihyro-2H-pyran in CAP, (b) the 5-aminoribose in CAR, and (c) the *meta*-tyrosine moiety in MUR bind to the uridine-adjacent pocket through H-bonds and H–H bonding interactions with residues Thr75, Asn190, Asp193, Gly264, and Asp265. Residues are shown in ball and sticks and each inhibitor is depicted in licorice.

backbone carbonyl oxygen, resulting in the appearance of N16–H1···O, N16–H1···Oδ2, and N16–H161···Oδ1 H-bonds in CAR–Asn190 and CAR–Asp265 pairs (Figure 8b). The amide nitrogen of *meta*-tyrosine moiety concurrently donates its hydrogen atom (H332) to the Oδ1 nucleus both in Asn190 and in Asp265. Therefore, N33–H332…Oδ1 H-bonds are formed in MUR–Asn190 and MUR–Asp265 pairs (Figure 8c). Even though there is no H-bonding interaction between CAP and Asn190, O31–H311···Oδ1 is characterized in the CAP–Asp265 pair (Figure 8a). Likewise, Asn190 interacts with CAR and MUR via H-bonds of C20–H202···O and C27–H272···O, respectively (Figure 8b–c). Of these, N16–H161···Oδ1 with an $|E_{HB}|$ of 21.12 kJ/mol and a length of 2.13 Å in the CAR–Asp265 pair is a moderate H-bond, while the other seven interactions are within the range of weak H-bonds (Table 2). Except for specified interactions, the 5-aminoribosyl moiety forms two additional weak H-bonds with Phe262 and Ser268 (Table 2). Analogous to these three inhibitors, similar H-bonds have been detected in the MD2–Asn190, MD2–Asp193, MD2–Phe262, and MD2–Ser268 pairs as well as in the TUN–Asn172 and TUN–Asp175 pairs (in $MraY_{CB}$).[41,42]

Due to the spatial orientation of the caprolactam moiety of CAP relative to Lys121, Leu122, and Lys125, its methylene groups are connected to the side chains of these residues by several H···H bond paths. As a consequence, a special type of van der Waals interaction called hydrogen–hydrogen bonding (H–H bonding) interaction[37] emerges in each H···H BCP. The topological parameters extracted from the H···H BCPs in all three QM models accompanying the absolute values of H–H bonding interaction energies, $|E_{H-H}|$, are provided in Table 3. Since weak Cε–Hε1···O29 in the CAP–Lys121 pair is only H-bond found in this binding site, the caprolactam binding pocket is mainly stabilized by the H–H bonding interactions among Lys121, Leu122, Lys125, and caprolactam (Figure 9a). In the QM model I, C24–H242···Hγ1–Cγ ($|E_{H-H}| = 40.18$ kJ/mol) and C23–H231···Hε1–Cε ($|E_{H-H}| = 35.28$ kJ/mol) in the CAP–Lys121 pair are the strongest H–H bonding interactions. Among residues enclosed the aliphatic tail of CAR (Figure 5c), Ile130, Asn187, Leu191, Thr299, and Ile303 are also involved in the multiple weak H–H bonding interactions with this moiety (Table 3). Moreover, C31–H312···Nδ2 with an $|E_{HB}|$ of 7.41 kJ/mol in the CAR–Asn187 pair is only H-bond that is characterized in this hydrophobic pocket (Figure 9b). Likewise, Leu191 and Val302 interact with the tetrapeptide portion of MUR through the H–H bonding interactions (Figure 9c). In the QM model III, C27–H273···Hα–Cα with an $|E_{H-H}|$ of 16.05 kJ/mol in the

Table 3. The Topological Parameters of the Electron Density in Various H···H BCPs Relevant to CAP-Residue, CAR-Residue, and MUR-Residue Pairs of QM Models I, II, and III Were Assessed at the M06-2X/6-31G** Level.[a]

Inhibitor-Residue Pair	H–H Bonding Interaction	d	ρ_{BCP}	$\nabla^2\rho_{BCP}$	H_{BCP}	$\lvert E_{H-H}\rvert$
CAP–Thr75	C22–H221···Hγ23–Cγ2	2.21	0.0073	0.0258	−0.0025	5.03
CAP–Thr75	C26–H261···Hγ23–Cγ2	2.31	0.0070	0.0250	−0.0022	4.65
CAP–Lys121	C24–H242···Hγ1–Cγ	1.53	0.0358	0.1102	−0.0321	40.18
CAP–Lys121	C23–H231···Hε1–Cε	1.67	0.0315	0.1207	−0.0252	35.28
CAP–Lys121	C13–H131···Hζ1–Mζ	2.45	0.0045	0.0158	−0.0012	2.80
CAP–Leu122	C24–H242···Hα–Cα	2.62	0.0033	0.0106	−0.0007	1.74
CAP–Leu122	C25–H251···Hδ22–Cδ2	2.34	0.0068	0.0245	−0.0022	4.59
CAP–Leu122	C25–H252···Hδ22–Cδ2	2.12	0.0089	0.0300	−0.0037	6.55
CAP–Lys125	C26–H262···Hε1–Cε	2.00	0.0105	0.0353	−0.0053	8.47
CAP–Lys125	C25–H252···Hδ1–Cδ	2.57	0.0038	0.0128	−0.0009	2.19
CAR–Lys70	O04–H041···Hβ1–Cβ	2.16	0.0062	0.0243	−0.0021	4.47
CAR–Ile130	C38–H383···Hγ12–Cγ1	2.18	0.0084	0.0293	−0.0030	5.86
CAR–Asn187	C33–H331···Hδ22–Mδ2	2.14	0.0067	0.0235	−0.0026	4.84
CAR–Asn187	C29–H292···Hβ1–Cβ	2.75	0.0022	0.0073	−0.0003	1.10
CAR–Leu191	C20–H202···Hα–Cα	2.66	0.0028	0.0093	−0.0005	1.46
CAR–Leu191	C27–H271···Hδ21–Cδ2	2.27	0.0084	0.0301	−0.0030	5.91
CAR–Leu191	C25–H251···Hδ12–Cδ1	2.00	0.0119	0.0396	−0.0061	9.68
CAR–Asp193	C11–H111···Hβ1–Cβ	2.39	0.0052	0.0181	−0.0013	3.15
CAR–Phe262	O04–H041···Hε2–Cε2	2.58	0.0046	0.0152	−0.0011	2.63
CAR–Gly264	C10–H101···Hα2–Cα	1.98	0.0107	0.0331	−0.0056	8.52
CAR–Thr299	C37–H372···Hγ21–Cγ2	2.01	0.0112	0.0373	−0.0054	8.79
CAR–Ile303	C35–H351···Hδ1–Cδ	2.21	0.0074	0.0248	−0.0025	4.93
MUR–Leu191	C15–H151···Hδ11–Cδ1	2.03	0.0123	0.0446	−0.0058	9.99
MUR–Leu191	C27–H273···Hδ13–Cδ1	2.28	0.0066	0.0239	−0.0020	4.32
MUR–Leu191	C27–H273···Hα–Cα	1.75	0.0168	0.0481	−0.0123	16.05
MUR–Asp193	C29–H292···H–M	2.66	0.0025	0.0085	−0.0003	1.22
MUR–Asp193	C40–H401···Hβ1–Cβ	2.30	0.0056	0.0193	−0.0017	3.55
MUR–Val302	C16–H161···Hγ22–Cγ2	2.06	0.0111	0.0412	−0.0046	8.50

[a] The H···H distance (d) is in Angstrom (Å). All ρ_{BCP}, $\nabla^2\rho_{BCP}$, and H_{BCP} parameters are in atomic units (a.u.). $\lvert E_{H-H}\rvert$ is in kJ/mol.

MUR–Leu191 pair is the strongest H–H bonding interaction (Table 3).

The QTAIM analysis reveals that the imidazole ring of His325 forms a hydrogen bond of a common type with the carbonyl oxygen both of carboxyl group of the diazepanone and of the urea dipeptide motif (Figure 9b–c). Nε2–Hε2···O42 in the CAR–His325 pair has a length of 1.54 Å and an angle of 151.67°, whereas the length and angle of Nε2–Hε2···O23 in the MUR–His325 pair are 1.91 Å and 159.24°, respectively. Additionally, the $\lvert E_{HB}\rvert$ (84.46 kJ/mol) of the former H-bond is more than three times greater than that (26.06 kJ/mol) of the latter H-bond. His325 thus binds more strongly to the diazepanone than to the urea dipeptide motif. Indeed, Nε2–Hε2···O42 between His325 and CAR is the strongest H-bond in QM model II because the largest values of ρ_{BCP} (0.0629 a.u.) and $\nabla^2\rho_{BCP}$ (0.2286 a.u.) belong to this strong H-bond (Table 2). In the QM model I, there is no H-bond between CAP and His325 because they are remote from together.[10] His325 interacts indirectly with the L-epicapreomycidine moiety of MD2 through a water-mediated hydrogen-bonded (H-bonded) network.[8,41] The corresponding residue in $MraY_{CB}$ (His291) directly engages in a moderate H-bond (Nε2–Hε2···O41) with the GlcNAc moiety of TUN.[42] The urea dipeptide motif also binds to Ala321 through three weak H-bonds of N–H···O20, N09–H091···O, and C17–H171···O (Figure 9c and Table 2). On the contrary, this residue participates in a strong H-bond (N47–H471···O) with the L-epicapreomycidine moiety and a moderate H-bond (N50–H501···O) with the L-valine.[41] Ala321 hence connects with MD2 much stronger than with MUR.

As discussed here, we described the characteristics of each H-bond detected in the pertinent active site on the basis of its BCP properties and geometrical parameters. In fact, the H-bond length is a parameter to summarize the essential features of the H-bonding interaction via its implicit relationship with the topological features of ρ_{BCP}.[78] It is remarkable that we find an excellent inverse linear correlation between the ln $\lvert E_{HB}\rvert$ values and the distances of H-bonds identified in the inhibitor-residue pairs inside the active site of each MraY-inhibitor (Figures S9–

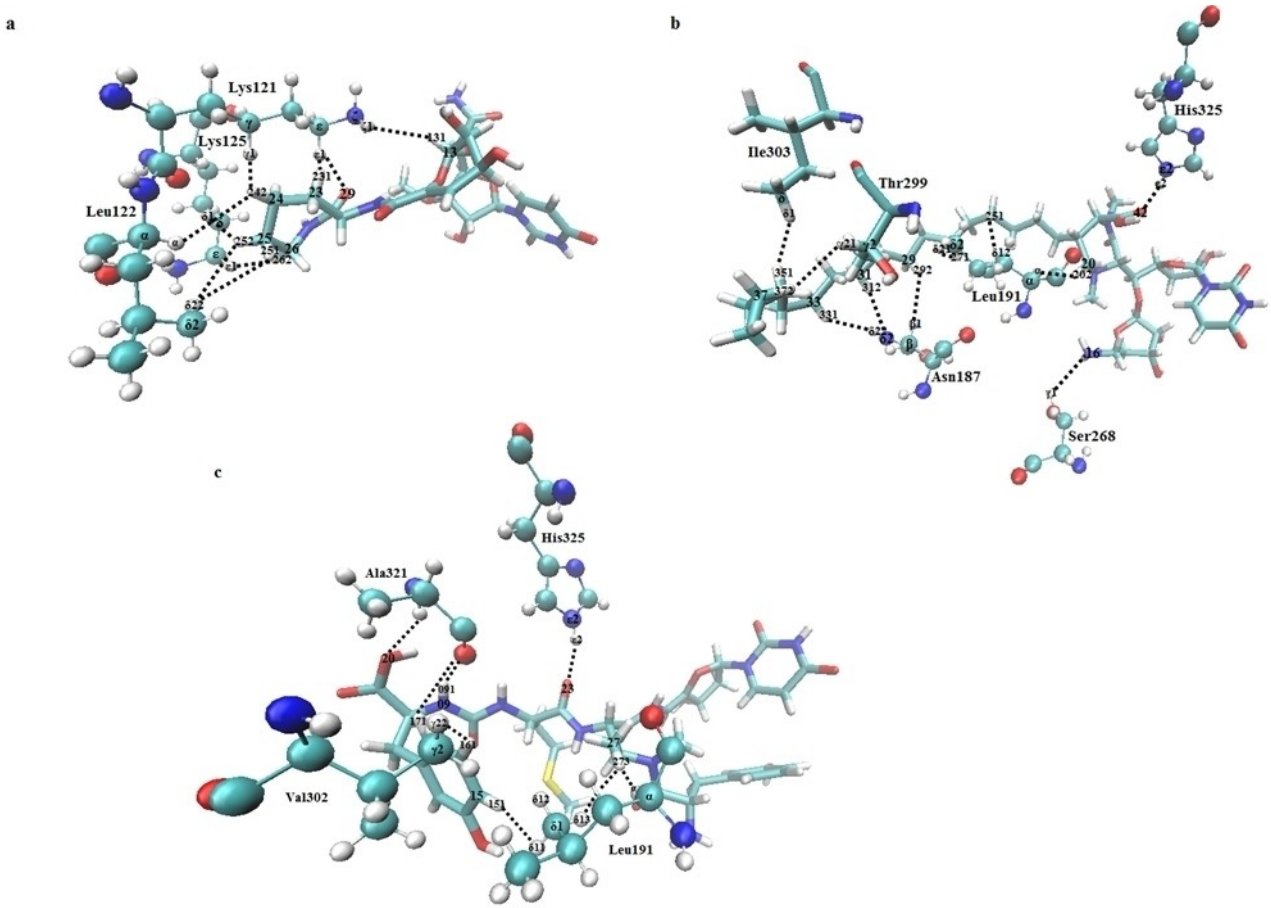

Figure 9. (a) The caprolactam moiety of CAP, (b) the diazepanone and aliphatic tail moieties of CAR, and (c) the tetrapeptide moiety of MUR are involved in H–H bonding interactions and H-bonds with the neighboring residues. Residues are shown in ball and sticks and each inhibitor is depicted in licorice.

S13). One of these linear relationships, pertaining to the CAP-residue pairs in the QM model I, is described by the following regression equation

$$\ln |E_{HB}| = -2.16\, d_{H\cdots O} + 7.56 \quad (10)$$

$$(R^2 = 0.976)$$

The negative slope in all cases affirms that the shorter H-bond length is associated with the stronger H-bonding interaction. These findings are in excellent agreement with our previous studies.[89–92]

It is worth stressing that the experimental studies on the $MraY_{AA}$-inhibitors have predicted the key roles of residues Lys70, Thr75, Asn190, Asp193, Asp196, Gly264, Asp265, Ala321, and His325 in binding of the relevant inhibitor to its binding pocket via H-bonding interactions.[10] Our QTAIM analysis, which complemented the experimental findings, detected not only the predicted H-bonds, and even the additional H-bonds, in each inhibitor binding pocket but also defined various aspects of these interactions, namely their strengths, nature, and other characteristics, in terms of the electron density topological features at the HBCPs.

Finally, the QTAIM outcomes show that although the total estimated $|E_{HB}|$ amounts relevant to the H-bonding interactions (533.92 kJ/mol) of the CAP-residue pairs are higher than those (417.51 kJ/mol) of the CAR-residue pairs and are about twice those (268.66 kJ/mol) of the TUN-residue pairs[42] and even are almost three times greater than those (194.20 kJ/mol) of the MUR-residue pairs, these energies are smaller than those (828.58 kJ/mol) of the MD2-residue pairs.[41] As a consequence, the MraY active site residues have the strongest H-bonding interactions with muraymycin D2.

Identification of CT Interactions of Inhibitor–Residue Pairs in the QM Models I, II, and III by the NBO Analysis

The QTAIM analysis delineated diverse H-bond characteristics of each inhibitor with its neighboring residues in the QM models I, II, and III. In the following, the strength of local orbitals of the partner atoms involving in each of these H-bonds are classified on the basis of the second-order stabilization energy, $E^{(2)}$, evaluated by the second-order perturbation theory in the framework of NBO analysis.[39,40,69] Table 4 presents the stabilization energies and the magnitude of the transferred charges, q_{CT},[40] of CT interactions occurred in all three QM models.

Table 4. The NBO Results of Local Orbitals Involving in Donor-Acceptor Interactions in CAP-Residue, CAR-Residue, and MUR-Residue Pairs of QM Models I, II, and III Were Calculated at the M06-2X/6-31G** Level.

Electron Donor	Electron Acceptor	Charge Transfer	$E^{(2)}$ (kJ/mol)	$q_{n_B \rightarrow \sigma^*_{A<C-H}}(e)$
CAP	Lys70	$n_{O40} \rightarrow \sigma^*_{C\varepsilon-H\varepsilon1}$	8.74	0.0029
CAP	Lys70	$n_{O39} \rightarrow \sigma^*_{N\zeta-H\zeta3}$	109.66	0.0680
CAR	Lys70	$n_{O52} \rightarrow \sigma^*_{C\delta-H\delta1}$	4.64	0.0027
CAR	Lys70	$n_{O52} \rightarrow \sigma^*_{N\zeta-H\zeta2}$	18.03	0.0082
CAP	Thr75	$n_{O20} \rightarrow \sigma^*_{O\gamma1-H\gamma1}$	33.76	0.0094
CAP	Gly194	$n_{O10} \rightarrow \sigma^*_{C\alpha-H\alpha2}$	7.70	0.0022
CAR	Gly194	$n_{O47} \rightarrow \sigma^*_{C\alpha-H\alpha2}$	3.01	0.0013
CAP	Asp196	$n_{O36} \rightarrow \sigma^*_{C\alpha-H\alpha}$	24.35	0.0105
CAR	Asp196	$n_{O56} \rightarrow \sigma^*_{C\alpha-H\alpha}$	6.69	0.0030
CAR	Asn255	$n_{O56} \rightarrow \sigma^*_{N\delta2-H\delta21}$	13.89	0.0039
CAR	Phe262	$n_{O14} \rightarrow \sigma^*_{C\beta-H\beta1}$	2.68	0.0012
CAP	Gly264	$n_{O30} \rightarrow \sigma^*_{N-H}$	27.66	0.0077
CAP	Gly264	$n_{O31} \rightarrow \sigma^*_{C\alpha-H\alpha2}$	2.80	0.0010
CAR	Gly264	$n_{O12} \rightarrow \sigma^*_{N-H}$	20.79	0.0063
CAR	Gly264	$n_{O12} \rightarrow \sigma^*_{C\alpha-H\alpha2}$	5.98	0.0025
CAR	Ser268	$n_{N16} \rightarrow \sigma^*_{O\gamma-H\gamma}$	8.12	0.0033
MUR	Ala321	$n_{O20} \rightarrow \sigma^*_{N-H}$	6.15	0.0019
CAR	His325	$n_{O42} \rightarrow \sigma^*_{N\varepsilon2-H\varepsilon2}$	101.21	0.0270
MUR	His325	$n_{O23} \rightarrow \sigma^*_{N\varepsilon2-H\varepsilon2}$	46.07	0.0134
Thr75	CAR	$n_{O\gamma1} \rightarrow \sigma^*_{O14-H141}$	32.89	0.0114
Thr75	CAR	$n_{O\gamma1} \rightarrow \sigma^*_{O12-H121}$	6.15	0.0022
Thr75	MUR	$n_{O\gamma1} \rightarrow \sigma^*_{O41-H411}$	22.18	0.0085
Asn187	CAR	$n_{N\delta2} \rightarrow \sigma^*_{C31-H312}$	6.95	0.0035
Asn190	CAR	$n_{O} \rightarrow \sigma^*_{N16-H1}$	8.66	0.0037
Asn190	CAR	$n_{O} \rightarrow \sigma^*_{C20-H202}$	4.64	0.0014
Asn190	MUR	$n_{O} \rightarrow \sigma^*_{C27-H272}$	8.79	0.0026
Asn190	MUR	$n_{O\delta1} \rightarrow \sigma^*_{N33-H332}$	9.12	0.0038
Asp193	CAP	$n_{O\delta1} \rightarrow \sigma^*_{C34-H341}$	5.61	0.0017
Asp193	CAP	$n_{O\delta1} \rightarrow \sigma^*_{O30-H301}$	81.00	0.0468
Asp193	CAP	$n_{O\delta2} \rightarrow \sigma^*_{O31-H311}$	76.86	0.0451
Asp193	CAR	$n_{O\delta2} \rightarrow \sigma^*_{O12-H121}$	32.38	0.0095
Asp193	CAR	$n_{O\delta2} \rightarrow \sigma^*_{O14-H141}$	11.84	0.0035
Asp193	MUR	$n_{O\delta2} \rightarrow \sigma^*_{C39-H391}$	34.43	0.0195
Asp196	CAP	$n_{O\delta1} \rightarrow \sigma^*_{N37-H371}$	41.76	0.0216
Asp196	CAR	$n_{O\delta1} \rightarrow \sigma^*_{N51-H511}$	40.58	0.0190
Asp196	MUR	$n_{O\delta1} \rightarrow \sigma^*_{N58-H581}$	115.27	0.0384
Asp265	CAP	$n_{O\delta1} \rightarrow \sigma^*_{O31-H311}$	5.10	0.0030
Asp265	CAR	$n_{O\delta1} \rightarrow \sigma^*_{N16-H161}$	20.67	0.0095
Asp265	CAR	$n_{O\delta2} \rightarrow \sigma^*_{N16-H1}$	3.47	0.0022
Asp265	MUR	$n_{O\delta1} \rightarrow \sigma^*_{N33-H332}$	8.08	0.0024
Ala321	MUR	$n_{O} \rightarrow \sigma^*_{N09-H091}$	11.09	0.0034

As already mentioned above, Nζ–Hζ3···O39 in the CAP–Lys70 pair is the strongest H-bond of CAP. The appearance of this H-bond is the consequence of the $n_{O39} \rightarrow \sigma^*_{N\zeta-H\zeta3}$ interaction with a q_{CT} of 0.0680 *e* and an $E^{(2)}$ of 109.66 kJ/mol. In agreement with the QTAIM outcomes, the NBO analysis reveals that this interaction possesses the largest q_{CT} and $E^{(2)}$ values compared to the other CT interactions of CAP in the QM model I (Table 4). Therefore, CAP has the strongest donor-acceptor interaction with Lys70. The n_{O52} lone pair of CAR uracil base concurrently donates the q_{CT} amounts of 0.0027 and

0.0082 *e* to the antibonding orbitals of $\sigma^*_{C\delta-H\delta1}$ and $\sigma^*_{N\zeta-H\zeta2}$ in Lys70, respectively, resulting in the formation of weak Cδ–Hδ1···O52 and moderate Nζ–Hζ2···O52 H-bonds in the CAR–Lys70 pair. In accordance with the $|E_{HB}|$ prediction, the $n_{O36}\rightarrow\sigma^*_{C\alpha-H\alpha}$ in the CAP–Asp196 pair is stronger than $n_{O56}\rightarrow\sigma^*_{C\alpha-H\alpha}$ in the CAR–Asp196 pair because $E^{(2)}$ (24.35 kJ/mol) of the former interaction is greater than that (6.69 kJ/mol) of the latter interaction. The $n_{O\delta1}$ of Asp196 separately overlaps with the antibonding orbitals of $\sigma^*_{N37-H371}$ (in CAP), $\sigma^*_{N51-H511}$ (in CAR), and $\sigma^*_{N58-H581}$ (in MUR). As $E^{(2)}$ (41.76 kJ/mol) of the $n_{O\delta1}\rightarrow\sigma^*_{N37-H371}$ in the CAP–Asp196 pair is only slightly higher than that (40.58 kJ/mol) of the $n_{O\delta1}\rightarrow\sigma^*_{N51-H511}$ in the CAR–Asp196 pair, they have nearly the same strengths. In line with the $|E_{HB}|$ prediction, the $n_{O\delta1}\rightarrow\sigma^*_{N58-H581}$ in the MUR–Asp196 pair is the strongest donor-acceptor interaction of MUR in the QM model III because the highest values of q_{CT} (0.0384 *e*) and $E^{(2)}$ (115.27 kJ/mol) in this model are attributed to this CT interaction (Table 4).

The NBO analysis explores that the hydroxyl group of Thr75 is an electron acceptor in the $n_{O20}\rightarrow\sigma^*_{O\gamma1-H\gamma1}$ interaction with CAP, whereas its $n_{O\gamma1}$ donates a charge of 0.0114 *e* to $\sigma^*_{O14-H141}$ and a charge of 0.0022 *e* to $\sigma^*_{O12-H121}$ of CAR as well as a charge of 0.0085 *e* to $\sigma^*_{O41-H411}$ of MUR. Of these, the $n_{O\gamma1}\rightarrow\sigma^*_{O12-H121}$ with an $E^{(2)}$ of 6.15 kJ/mol is the weakest interaction and the strength of the $n_{O20}\rightarrow\sigma^*_{O\gamma1-H\gamma1}$ with an $E^{(2)}$ of 33.76 kJ/mol is nearly identical to that of the $n_{O\gamma1}\rightarrow\sigma^*_{O14-H141}$ with an $E^{(2)}$ of 32.89 kJ/mol. Furthermore, the σ^*_{N-H} and $\sigma^*_{C\alpha-H\alpha2}$ in Gly264 accept the charges both from the n_{O30} and the n_{O31} in CAP and from the n_{O12} in CAR. On the other hand, the $n_{O\delta1}$ and $n_{O\delta2}$ in Asp193 donate their electrons to the antibonding orbitals of $\sigma^*_{C34-H341}$, $\sigma^*_{O30-H301}$, $\sigma^*_{O31-H311}$ (in CAP), $\sigma^*_{O12-H121}$, $\sigma^*_{O14-H141}$ (in CAR), and $\sigma^*_{C39-H391}$ (in MUR). Based on the $E^{(2)}$ and q_{CT} amounts of these CT interactions (Table 4), the CAP–Asp193 pair has the strongest donor-acceptor interactions relative to the other two pairs.

An infinitesimal charge (0.0030 *e*) is transferred from the $n_{O\delta1}$ of Asp265 to $\sigma^*_{O31-H311}$ in CAP with an $E^{(2}$ of 5.10 kJ/mol by forming weak O31–H311···Oδ1 H-bond. Asp265 also participates in two CT interactions of $n_{O\delta1}\rightarrow\sigma^*_{N16-H161}$ ($E^{(2)}=20.67$ kJ/mol) and $n_{O\delta2}\rightarrow\sigma^*_{N16-H1}$ ($E^{(2}=3.47$ kJ/mol) with CAR. As seen in Table 4, the $\sigma^*_{N33-H332}$ in MUR weakly overlaps with the $n_{O\delta1}$ both of Asn190 and of Asp265. The $n_{O\delta1}\rightarrow\sigma^*_{N33-H332}$ interactions thus exist in MUR–Asn190 and MUR–Asp265 pairs. The $\sigma^*_{N\varepsilon2-H\varepsilon2}$ in His325 interacts both with the n_{O42} of CAR and with the n_{O23} of MUR. The $n_{O42}\rightarrow\sigma^*_{N\varepsilon2-H\varepsilon2}$ interaction has an $E^{(2)}$ of 101.21 kJ/mol and a q_{CT} of 0.0270 *e*, while the q_{CT} and $E^{(2)}$ values of the $n_{O23}\rightarrow\sigma^*_{N\varepsilon2-H\varepsilon2}$ interaction are 0.0134 *e* and 46.07 kJ/mol, respectively. In agreement with the QTAIM findings, the former CT interaction is not only much stronger than the latter CT interaction but also it is the strongest donor-acceptor interaction of CAR in the QM model II (Table 4).

According to the NBO analysis, the whole estimated stabilization energies related to the CT interactions (613.04 kJ/mol) of the CAP-residue pairs are about twice both those (353.30 kJ/mol) of the CAR-residue pairs and those (310.39 kJ/mol) of the TUN-residue pairs[42] and are more than two times higher than those (264.14 kJ/mol) of the MUR-residue pairs but these energies are smaller than those (844.14 kJ/mol) of the MD2-residue pairs.[41] The MraY active site residues thus have the strongest donor-acceptor interactions with muraymycin D2.

Description of the Water-Mediated Interactions in Carbacaprazamycin Binding Pocket by QTAIM and NBO Analyses

The $MraY_{AA}$–CAR crystal structure shows the presence of two water molecules, numbering as water501 (Wt501) and water502 (Wt502), near the CAR uracil ring and residues Asp193, Leu195, and Met263.[10] Wt501 and Wt502 concomitant with these residues and inhibitor were selected as the QM model IV and all its atoms were optimized in the same manner as the other three QM models (Figure 10). Table 5 presents the characteristics of H-bonds and CT interactions of these two water molecules with carbacaprazamycin and the cited residues specified by QTAIM and NBO analyses.

Wt501 synchronously shares its hydrogen (H1) with the carbonyl oxygens of CAR uracil moiety and Leu195 and donates its other hydrogen (H2) to the Oδ1 nucleus of Asp193. Accordingly, its σ^*_{O-H1} receives very small charges of 0.0013 and 0.0017 *e* from the lone pair orbitals of n_{O56} in CAR and n_O in Leu195, respectively, whereas its σ^*_{O-H2} accepts a relatively large

Table 5. The Characteristics of H-Bonds and CT Interactions in the Fragment Pairs, Which Can Be CAR–Wt, Wt-Residue, and Wt–Wt Pairs, of the QM Model IV Were Calculated at the M06-2X/6-31G** Level.[a]

Fragment Pair	H-Bond	*d*	ρ_{BCP}	$\nabla^2\rho_{BCP}$	$\lvert E_{HB}\rvert$	Charge Transfer	$E^{(2)}$	$q_{n_B\rightarrow\sigma^*_{A<C->H}}(e)$
CAR–Wt501	O–H1···O56	2.35	0.0104	0.0390	10.86	$n_{O56}\rightarrow\sigma^*_{O-H1}$	4.73	0.0013
CAR–Wt502	C54–H541···O	2.49	0.0100	0.0301	9.07	$n_O\rightarrow\sigma^*_{C54-H541}$	6.95	0.0024
Wt501–Wt502	O–H2···O	1.95	0.0264	0.0755	27.60	$n_O\rightarrow\sigma^*_{O-H2}$	56.32	0.0226
Wt501–Asp193	O–H2···Oδ1	1.68	0.0413	0.1560	46.54	$n_{O\delta1}\rightarrow\sigma^*_{O-H2}$	86.73	0.0247
Wt501–Leu195	O–H1···O	2.32	0.0107	0.0403	11.28	$n_O\rightarrow\sigma^*_{O-H1}$	6.23	0.0017
Wt502–Asp193	O–H1···Oδ1	2.20	0.0176	0.0659	15.03	$n_{O\delta1}\rightarrow\sigma^*_{O-H1}$	8.12	0.0036
Wt502–Asp193	O–H1···Oδ2	1.83	0.0333	0.1033	34.94	$n_{O\delta2}\rightarrow\sigma^*_{O-H1}$	51.63	0.0223
Wt502–Met263	N–H···O	1.89	0.0285	0.0873	30.01	$n_O\rightarrow\sigma^*_{N-H}$	71.25	0.0252

[a] The H-bond length (*d*) is in Angstrom (Å). All ρ_{BCP} and $\nabla^2\rho_{BCP}$ parameters are in atomic units (a.u.). $\lvert E_{HB}\rvert$ and $E^{(2)}$ are in kJ/mol.

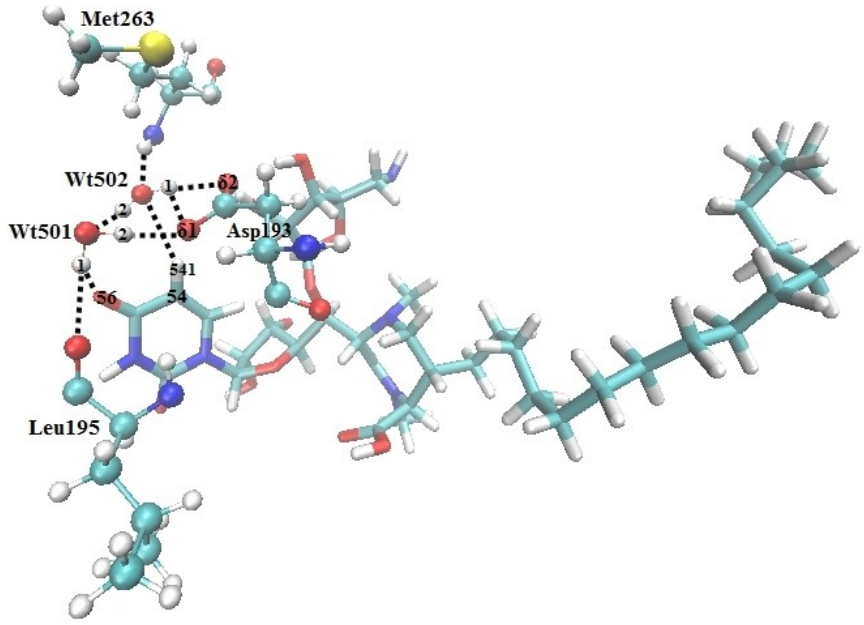

Figure 10. The QM model IV shows that the CAR uracil moiety is connected to residues Asp193, Leu195, and Met263 via H-bonded networks created by the hydrogen bridges of Wt501 and Wt502. Residues and water molecules are shown in ball and sticks and CAR is depicted in licorice.

q_{CT} of 0.0247 *e* from the $n_{O\delta1}$ of Asp193. Consequently, moderate H-bond of O–H2···Oδ1 with an $|E_{HB}|$ of 46.54 kJ/mol and a length of 1.68 Å is formed between Wt501 and Asp193 by occurring the $n_{O\delta1}\rightarrow\sigma^*_{O-H2}$ interaction with an $E^{(2)}$ of 86.73 kJ/mol between them, but O–H1···O56 and O–H1···O in CAR–Wt501 and Wt501–Leu195 pairs are weak H-bonds (Figure 10 and Table 5). Moreover, O–H2···O with an $|E_{HB}|$ of 27.60 kJ/mol is found in the Wt501–Wt502 pair due to transfer a charge of 0.0226 *e* from the n_O of Wt501 into the σ^*_{O-H2} in Wt502 with an $E^{(2)}$ of 56.32 kJ/mol.

Synchronous transfer of electrons from the n_O of Wt502 into the antibonding orbitals of $\sigma^*_{C54-H541}$ in CAR and σ^*_{N-H} in Met263 is the reason for the existence of weak C54–H541···O H-bond in the CAR–Wt502 pair and moderate N–H···O H-bond in the Wt502–Met263 pair (Table 5). Due to overlap the σ^*_{O-H1} of Wt502 with both the $n_{O\delta1}$ and the $n_{O\delta2}$ in Asp193, two bond paths of H1···Oδ1 and H1···Oδ2 are observed in the Wt502–Asp193 pair (Figure 10). As the $|E_{HB}|$ (34.94 kJ/mol) of O–H1···Oδ2 is higher than that (15.03 kJ/mol) of O–H1···Oδ1, the former H-bond is stronger than the latter H-bond. Although, none of these residues are able to form H-bonds with each other or with the CAR uracil moiety, they are connected together by mediating Wt501 and Wt502. Their hydrogen bridges hence create H-bonded networks of N–H···O–H2···O–H1···O56 in Met263–Wt502–Wt501–CAR, C54–H541···O–H2···O–H1···O in CAR–Wt502–Wt501–Leu195, Oδ1···H1–O–H2···O–H1···O56 and Oδ2···H1–O–H2···O–H1···O56 in Asp193–Wt502–Wt501–CAR, C54–H541···O–H1···Oδ1 and C54–H541···O–H1···Oδ2 in CAR–Wt502–Asp193, C54–H541···O···H–N in CAR–Wt502–Met263, and O···H1–O–H1···O56 in Leu195–Wt501–CAR (Figure 10). Indeed, Asp193, Leu195, and Met263 interact indirectly with the CAR uracil moiety via the mediated pathways arising from the hydrogen bridges of these water molecules and thereby enhance the strengths of CAR–Wt501 and CAR–Wt502 interactions. We therefore conclude that Wt501 and Wt502 play the central roles in the binding stability of the CAR uracil moiety to the $MraY_{AA}$–CAR active site by forming H-bonds with both CAR and residues Asp193, Leu195, and Met263. It is worth highlighting that the uracil binding pocket within the active sites of $MraY_{AA}$–MD2[41] and $MraY_{CB}$–TUN[42] are also stabilized by the water-mediated H-bonded networks.

A Comparison of the Intermolecular Interaction Strengths of Inhibitor-Residue Pairs of QM Models I, II, and III

In the previous sections, we determined the most important characteristics of H-bonds and CT interactions of each inhibitor with its neighboring residues in the pertinent model by the QTAIM and NBO analyses. The strengths of these interactions were classified into three types: weak, moderate, and strong interactions based on the magnitude of their H-bond and stabilization energies, which are considered as appropriate energy criteria. In all four models, most of the H-bonds and CT interactions were concentrated in the uridine binding and the uridine-adjacent pockets. As discussed above, these pockets contain residues Lys70, Thr75, Asn190, Asp193, Gly194, Leu195, Asp196, Asn255, Phe262, Gly264, and Asp265. In addition to H-bonds, it is apparent that these residues, according to the chemical properties of their side chains, are able to interact with the different moieties of CAP, CAR, and MUR through other types of noncovalent intermolecular interactions, namely electrostatic and van der Waals interactions. Due to the presence of

a localized positive charge on Lysine side chain amino group as well as because of the existence of a delocalized negative charge on Aspartate side chain carboxylate oxygens, charge–dipole and dipole–dipole interactions are hence the most important electrostatic interactions occurring in the charged pairs of CAP–Lys70, CAR–Lys70, CAP–Asp193, CAR–Asp193, MUR–Asp193, CAP–Asp196, CAR–Asp196, MUR–Asp196, CAP–Asp265, CAR–Asp265, and MUR–Asp265. Because of the uncharged and polar nature of the side chains of Asparagine and Threonine, the dipole–dipole interactions also appear in the polar pairs of CAP–Thr75, CAR–Thr75, MUR–Thr75, CAP–Asn190, CAR–Asn190, MUR–Asn190, CAR–Asn255, and MUR–Asn255. Furthermore, the nonpolar side chains of residues Gly194, Leu195, Phe262, and Gly264 are instantly induced by the dipole moments on functional groups of the uridine, 3,4-dihydroxy-3,4-dihyro-2H-pyran, 5-aminoribosyl, and *meta*-tyrosine moieties, resulting in the appearance of the induced (temporary) dipole moments in their side chains. Consequently, the dipole-induced dipole interactions take place in CAP–Gly194, CAR–Gly194, MUR–Gly194, CAP–Leu195, CAR–Leu195, MUR–Leu195, CAP–Phe262, CAR–Phe262, MUR–Phe262, CAP–Gly264, CAR–Gly264, and MUR–Gly264 pairs. The intermolecular interaction energy of each inhibitor-residue pair can be calculated by the supermolecule approach and corrected for basis set superposition error (BSSE) using the counterpoise (CP) procedure suggested by Boys and Bernardi.[93] The absolute values of the counterpoise-corrected intermolecular interaction energies, $|E_{interaction}|$, BSSE energies, and dipole moments of the inhibitor-residue pairs of QM models I, II, and III are collected in Table 6.

The QTAIM and NBO analyses confirmed that capuramycin has the strongest H-bond and donor-acceptor interaction with Lys70. In addition to H-bond, large $|E_{interaction}|$ (138.47 kJ/mol) of the CAP–Lys70 pair means significant contribution of electrostatic interactions to the intermolecular interactions of this positively charged pair. It would be reasonable to suggest that Lys70 is one of the crucial residues in the capuramycin binding pocket because it plays a fundamental role in locating the CAP uridine moiety into the uridine binding pocket through strong H-bonding, charge-dipole, and dipole-dipole interactions. Similarly, the $|E_{interaction}|$ (107.24 kJ/mol) of the MD2–Lys70 pair[41] signifies the main role of Lys70 in placing the MD2 uridine moiety in the muraymycin D2 binding pocket. In contrast, the $|E_{interaction}|$ (63.48 kJ/mol) of the CAR–Lys70 pair proves its influence decrease on the CAR uracil base binding to the carbacaprazamycin binding pocket. In the $MraY_{AA}$–MUR complex structure,[10] since Lys70 is situated far away from the 3′-hydroxymureidomycin A binding pocket, it has no interaction with MUR.

It is evident from the results in Table 6 that the highest $|E_{interaction}|$ value in each QM model is assigned to the inhibitor-Asp193 pair. As a result, Asp193 is an indispensable residue in the $MraY_{AA}$ uridine-adjacent pocket, which plays an essential role in locating the 3,4-dihydroxy-3,4-dihyro-2H-pyran of CAP, the 5-aminoribose of CAR, or the *meta*-tyrosine of MUR in this pocket through moderate and weak H-bonds accompanying strong charge–dipole and dipole–dipole interactions. Similarly, in the muraymycin D2 binding pocket,[41] Asp193 showed the same behaviour for the 5-aminoribosyl moiety binding to the uridine-adjacent pocket. Among four inhibitor-Asp193 pairs, the largest $|E_{interaction}|$ (194.40 kJ/mol) is observed in the CAP–Asp193 pair; Asp193 has thus the strongest intermolecular interactions with capuramycin (Table 6).

In spite of the different strengths of H-bonds in the CAP–Asp196 pair and the CAP–Asp265 pair (Table 2), $|E_{interaction}|$ (103.71 kJ/mol) in the former pair is only slightly greater than that (103.61 kJ/mol) in the latter pair. Consequently, the strengths of their intermolecular interactions are equivalent, albeit the principal nature of the CAP–Asp265 interactions is the type of charge–dipole and dipole–dipole interactions. As the $|E_{interaction}|$ (70.37 kJ/mol) in the CAR–Asp196 pair is higher than that (60.66 kJ/mol) in the CAR–Asp265 pair, intermolecular interactions in the former pair are stronger than those in the latter pair. According to the $|E_{interaction}|$ values (Table 6), the strength of the MUR–Asp265 interactions is greater than that of the MUR–Asp196 interactions.

In the polar pairs of CAP–Thr75, CAR–Thr75, MUR–Thr75, CAR–Asn190, MUR–Asn190, and CAR–Asn255, H-bonds are the most important intermolecular interactions in these pairs because the $|E_{interaction}|$ in each of them is approximately equal to or close to its $|E_{HB}|$ component (Tables 2 and 6). Small $|E_{interaction}|$ values of the inhibitor-Gly194, inhibitor-Leu195, and inhibitor-Phe262 pairs are indicative of the existence of weak intermolecular interactions in them (Table 6). Although no H-bonds were found in the MUR–Arg320, CAP–Asn190, MUR–Asn255, MUR–Gln305, CAP–His325, CAP–Ala259, CAR–Ala259, CAP–Met263, CAR–Met263, MUR–Met263, CAR–Ala321, CAR–Pro322, and MUR–Pro322 pairs (Table 2), each residue interacts weakly with its partner inhibitor via charge–dipole, dipole–dipole, and dipole–induced dipole interactions (Table 6).

Except for the H–H bonding interactions, because of the presence of two positively charged residues Lys121 and Lys125 in the caprolactam binding pocket, charge–dipole, dipole–dipole, and dipole–induced dipole interactions are expected to play crucial roles in preserving and stabilizing this pocket. The $|E_{interaction}|$ values of 67.77 (in the CAP–Lys121 pair) and 60.17 kJ/mol (in the CAP–Lys125 pair) confirm the importance of the electrostatic interactions to the caprolactam binding to its pocket. In addition to H–H bonding interactions, the aliphatic tail of carbacaprazamycin interacts with nonpolar side chains of residues Ile130, Phe134, Phe180, Val183, Gly184, Leu191, Val296, Thr299, Val302, Ile303, and Ile306 via another type of van der Waals interactions named the hydrophobic interactions. Since weak H–H bonding and hydrophobic interactions are the main contributors to the CAR-nonpolar residue interactions, the $|E_{interaction}|$ values of these CAR-nonpolar residue pairs are very small (Table 6).

In the TM9b/Loop E pocket, since the strength of the CAR–His325 interactions ($|E_{interaction}| = 91.89$ kJ/mol) is comparable to that of Nε2–Hε2···O42 H-bond ($|E_{HB}| = 84.46$ kJ/mol) in the CAR–His325 pair, this strong H-bond is dominant intermolecular interaction in this pair. Besides, dipole–dipole interaction between the imidazole ring of His324 and the carboxyl group

Table 6. The Absolute Values of the Counterpoise-Corrected Intermolecular Interaction Energies, the BSSE Energies, and Dipole Moments of CAP-Residue, CAR-Residue, and MUR-Residue Pairs of QM Models I, II, and III Were Evaluated at the M06-2X/6-31G** Level.

Model	Inhibitor-Residue Pair	$\lvert E_{interaction} \rvert$ (kJ/mol)	BSSE Energy (kJ/mol)	dipole (debye)
Model I	CAP–Lys70	138.47	9.01	14.71
	CAP–Thr75	35.03	15.78	3.30
	CAP–Lys121	67.77	15.53	20.89
	CAP–Leu122	3.35	2.17	4.17
	CAP–Lys125	60.17	2.00	50.97
	CAP–Asn190	1.18	0.00	1.15
	CAP–Asp193	194.40	36.96	15.03
	CAP–Gly194	18.80	14.67	12.50
	CAP–Leu195	8.60	13.41	11.09
	CAP–Asp196	103.71	20.69	40.38
	CAP–Ala259	1.05	0.09	11.69
	CAP–Phe262	24.68	17.85	3.58
	CAP–Met263	11.54	8.35	11.78
	CAP–Gly264	45.84	11.82	5.37
	CAP–Asp265	103.61	11.09	25.11
	CAP–His325	2.93	0.02	11.37
Model II	CAR–Lys70	63.48	10.16	40.30
	CAR–Thr75	31.72	9.09	3.34
	CAR–Ile130	2.43	1.75	7.63
	CAR–Phe134	2.34	2.04	6.69
	CAR–Phe180	2.50	3.09	5.08
	CAR–Val183	3.25	1.51	4.69
	CAR–Gly184	4.89	3.50	3.68
	CAR–Ser185	1.40	1.23	1.68
	CAR–Asn187	5.17	4.06	8.64
	CAR–Asn190	15.93	15.95	10.23
	CAR–Leu191	7.48	8.70	3.17
	CAR–Asp193	190.55	28.82	26.37
	CAR–Gly194	3.54	13.32	4.19
	CAR–Leu195	6.64	9.91	6.07
	CAR–Asp196	70.37	19.84	49.48
	CAR–Asn255	12.05	4.47	3.18
	CAR–Ala259	1.93	1.69	5.84
	CAR–Phe262	21.04	14.49	6.96
	CAR–Met263	2.65	5.27	5.13
	CAR–Gly264	7.91	9.76	4.68
	CAR–Asp265	60.66	20.13	30.76
	CAR–Ser268	18.00	3.90	5.68
	CAR–Val296	1.25	0.46	3.38
	CAR–Thr299	1.55	1.95	5.94
	CAR–Val302	3.06	1.10	5.38
	CAR–Ile303	3.53	2.37	5.93
	CAR–Ile306	0.84	0.53	4.94
	CAR–Ala321	3.74	1.73	4.08
	CAR–Pro322	4.10	3.08	5.05
	CAR–His324	33.78	4.47	7.26
	CAR–His325	91.89	7.06	7.29
Model III	MUR–Thr75	19.54	9.73	4.02

Table 6. continued

Model	Inhibitor-Residue Pair	$\lvert E_{interaction} \rvert$ (kJ/mol)	BSSE Energy (kJ/mol)	dipole (debye)
	MUR–Asn190	32.93	14.75	10.99
	MUR–Leu191	6.91	7.33	11.52
	MUR–Asp193	62.54	33.29	26.23
	MUR–Gly194	13.96	8.15	2.47
	MUR–Leu195	13.89	9.92	4.16
	MUR–Asp196	45.35	15.35	42.42
	MUR–Asn255	2.76	1.42	7.78
	MUR–Phe262	16.90	15.30	4.43
	MUR–Met263	4.49	4.93	9.27
	MUR–Gly264	5.95	4.87	5.43
	MUR–Asp265	55.43	8.88	25.59
	MUR–Val302	0.75	4.23	12.67
	MUR–Gln305	18.20	5.41	13.62
	MUR–Arg320	10.77	4.04	30.23
	MUR–Ala321	36.84	14.05	9.81
	MUR–Pro322	7.77	4.79	12.93
	MUR–His325	23.46	5.33	13.87

of diazepanone is another effective interaction in stabilizing this pocket. As the $\lvert E_{interaction} \rvert$ (36.84 kJ/mol) in the MUR–Ala321 pair is larger than that (23.46 kJ/mol) in the MUR–His325 pair, the urea dipeptide motif has stronger intermolecular interactions with Ala321 than with His325.

According to the counterpoise-corrected intermolecular interaction energies, the sum of the $\lvert E_{interaction} \rvert$ values associated to the CAP-residue pairs is equal to 821.14 kJ/mol. The whole of these energies for the MD2-residue pairs,[41] the TUN-residue pairs,[42] the CAR-residue pairs, and the MUR-residue pairs are 741.19, 695.65, 679.68, and 378.44 kJ/mol, respectively. As a consequence, although the QTAIM and NBO analyses confirmed that the sums of the H-bonding energies and stabilization energies related to the H-bonds and CT interactions detected in the muraymycin D2 binding pocket are the highest compared to those found in the other inhibitor binding pockets, the calculate intermolecular interaction energies prove that the capuramycin binding pocket is the most stable pocket among the five MraY inhibitors. We hence conclude that even though H-bonding interactions play essential roles in forming the MraY-inhibitor complex structures, the influences of electrostatic and van der Waals interactions on the binding stabilities of these inhibitors to the MraY active sites are undeniable. The binding strengths of these five inhibitors to the MraY active sites in terms of the total $\lvert E_{interaction} \rvert$ amounts decrease as follows: capuramycin > muraymycin D2 > tunicamycin > carbacaprazamycin > 3′-hydroxymureidomycin A. Hence, there is an excellent agreement between the MD simulation results and the QM calculation outcomes. On the basis of the DFT QM/MM MD calculations, we conclude that in-depth information obtained from the present work not only can help to redesign the structures of studied inhibitors to improve their recognition properties but it can also be used in the design of new generations of nucleoside antibiotics.

Conclusions

The atomic coordinates of low-resolution crystal structures of $MraY_{AA}$-capuramycin, $MraY_{AA}$-carbacaprazamycin, and $MraY_{AA}$-3′-hydroxymureidomycin A have been accurately optimized in the explicit solvent under periodic boundary conditions by using the hybrid QM/MM molecular dynamics simulations. Afterwards, QTAIM and NBO analyses at the M06-2X/6-31G** level were implemented on the inhibitor binding pocket (the QM model) of each optimized structure to achieve a comprehensive and detailed picture of the nature and strengths of intermolecular interactions of each nucleoside inhibitor with the $MraY_{AA}$ active site residues at the atomic level. Our QTAIM and NBO results revealed that the capuramycin, carbacaprazamycin, and 3′-hydroxymureidomycin A binding pockets have the hydrogen-bonding and charge transfer interactions in common types with strength ranging from van der Waals to covalent characters. In all three inhibitor binding pockets, most of these interactions were concentrated in the uridine binding and uridine-adjacent pockets. Moreover, since these two pockets are mainly constituted by positively charged, negatively charged, and polar residues, charge–dipole and dipole–dipole interactions play significant roles in their preservation and stabilization. It should be noted that the electrostatic interactions have considerable contributions to the intermolecular interactions of both the inhibitor–Asp193 pairs and the inhibitor–Asp265 pairs.

In each QM model, the inhibitor has the strongest intermolecular interactions with Asp193 because the inhibitor-Asp193 pair has the highest $\lvert E_{interaction} \rvert$ compared to the other

inhibitor–residue pairs of that model. Asp193 is thus one of the most important residues in each $MraY_{AA}$–inhibitor active site that provides the binding of the 3,4-dihydroxy-3,4-dihyro-2H-pyran of CAP, the 5-aminoribose of CAR, or the *meta*-tyrosine of MUR to the uridine-adjacent pocket through H-bonds and the electrostatic interactions. Residues Lys70, Thr75, Asn190, Gly194, Leu195, Asp196, Asn255, Gly264, and Asp265 are other crucial residues of the uridine binding and the uridine-adjacent pockets that assist in their stabilities via multiple weak, moderate, and strong conventional and unconventional hydrogen bonds concomitant with charge–dipole, dipole–dipole, dipole–induced dipole, and hydrogen–hydrogen bonding interactions. Likewise, the $MraY_{AA}$ uridine binding pocket is stabilized by the π···π stacking interaction occurring between the aromatic ring of its Phe262 and the uracil base ring of each cited inhibitor. Besides, the water-mediated hydrogen-bonded networks play central roles in maintaining the position of the uracil moiety of carbacaprazamycin within this pocket.

The QTAIM analysis confirmed that Nζ–Hζ3···O39 H-bond between the uracil base and Lys70 is the strongest H-bonding interaction of capuramycin in the $MraY_{AA}$–CAP active site. Furthermore, the $|E_{interaction}|$ values proved that the CAP–Lys70 pair is the most stable positively charged inhibitor–residue pair in all three QM models. In the capuramycin binding pocket, Lys121, Leu122, and Lys125 ensure the caprolactam binding to the caprolactam binding pocket mainly via charge–dipole, dipole–dipole, dipole–induced dipole, and H–H bonding interactions. In the carbacaprazamycin binding pocket, the hydrophobic and H–H bonding interactions are the dominant intermolecular interactions among the aliphatic tail of carbacaprazamycin and nonpolar residues Ile130, Phe134, Phe180, Val183, Gly184, Leu191, Val296, Thr299, Val302, Ile303, and Ile306. Although strong H-bond of Nε2–Hε2···O42 in the CAR–His325 pair is only H-bond formed by the diazepanone in this binding pocket, it is the strongest H-bonding interaction of carbacaprazamycin in the $MraY_{AA}$–CAR active site. In the 3′-hydroxymureidomycin A binding pocket, Ala321 and His325 interact with the urea dipeptide motif through H-bonding, dipole–dipole, and dipole–induced dipole interactions.

Finally, energy analyses of the MraY-inhibitor interactions obtained from both MD simulations and QM calculations demonstrated that the $MraY_{AA}$-capuramycin binding is the most stable MraY-inhibitor binding among the five MraY inhibitors. The electrostatic interactions, particularly charge–dipole and dipole–dipole interactions in the CAP–Lys70, CAP–Asp193, CAP–Asp196, and CAP–Asp265 pairs, have considerable contributions to the total intermolecular interactions of the capuramycin binding pocket. It is worth stressing here that the information gained from our DFT QM/MM MD simulations is conducive to develop new potent MraY-targeted nucleoside antibiotics.

Supporting Information

Supporting Information contains topology entries of capuramycin, carbacaprazamycin, 3′-hydroxymureidomycin A, and muraymycin D2, Tables (S1–S6) pertaining to the parameter entries of these nucleoside inhibitors, Figures (S1–S13) displaying the QM models I, II, and III, the energy analyses of the MraY-inhibitor interactions, and linear relationship between ln $|E_{HB}|$ values and lengths of H-bonds detected in the inhibitor-residue pairs inside the inhibitor binding pockets.

Author Contributions

The manuscript was written through contributions of all authors. All authors have given approval to the final version of the manuscript. † Elahe K. Astani and Saeid MalekZadeh contributed equally to the work.

Acknowledgements

We acknowledge the support of computation facilities of the medical biotechnology department at the Pasteur Institute of Iran.

Conflict of Interests

The authors declare no conflict of interest.

Data Availability Statement

The data that support the findings of this study are available in the supplementary material of this article.

Keywords: $MraY_{AA}$-nucleoside inhibitor complex structures · hybrid QM/MM molecular dynamics simulations · QTAIM and NBO analyses · noncovalent intermolecular interactions · $MraY_{AA}$-inhibitor interaction energies

[1] T. D. H. Bugg, D. Braddick, C. G. Dowson, D. I. Roper, *Trends Biotechnol.* **2011**, *29*, 167–173.
[2] M. Winn, R. J. M. Goss, K. I. Kimura, T. D. H. Bugg, *Nat. Prod. Rep.* **2010**, *27*, 279–304.
[3] J. V. Heijenoort, *Nat. Prod. Rep.* **2001**, *18*, 503–519.
[4] H. Barreteau, A. Kovac, A. Boniface, M. Sova, S. Gobec, D. Blanot, *FEMS Microbiol. Rev.* **2008**, *32*, 168–207.
[5] W. G. Struve, F. C. Neuhaus, *Biochem. Biophys. Res. Commun.* **1965**, *18*, 6–12.
[6] J. S. Anderson, M. Matsuhashi, M. A. Haskin, J. L. Strominger, *Biochemistry.* **1965**, *53*, 881–889.
[7] D. S. Boyle, W. D. Donachie, *J. Bacteriol.* **1998**, *180*, 6429–6432.
[8] B. C. Chung, E. H. Mashalidis, T. Tanino, M. Kim, A. Matsuda, J. Hong, S. Ichikawa, S. Y. Lee, *Nature.* **2016**, *533*, 557–560.
[9] J. K. Hakulinen, J. Hering, G. Brändén, H. Chen, A. Snijder, M. Ek, P. Johansson, *Nat. Chem. Biol.* **2017**, *13*, 265–267.
[10] E. H. Mashalidis, B. Kaeser, Y. Terasawa, A. Katsuyama, D. Y. Kwom, K. Lee, J. Hong, S. Ichikawa, S. Y. Lee, *Nat. Commun.* **2019**, *10*, 2917.
[11] J. Hering, E. Dunevall, M. Ek, G. Brändén, *Drug Discovery Today* **2018**, *23*, 1426–1435.
[12] T. Koga, T. Fukuoka, N. Doi, T. Harasaki, H. Inoue, H. Hotoda, M. Kakuta, Y. Muramatsu, N. Yamamura, M. Hoshi, T. Hirota, *J. Antimicrob. Chemother.* **2004**, *54*, 755–760.
[13] C. T. Walsh, W. Zhang, *ACS Chem. Biol.* **2011**, *6*, 1000–1007.

[14] S. Malek Zadeh, M. H. Chen, Z. C. Wang, E. K. Astani, I. W. Lo, K. H. Lin, N. S. Hsu, K. Adhikari, S. Y. Lyu, H. Y. Tsai, Y. Terasawa, M. Y. Yabe, K. Yamamoto, S. Ichikawa, T. L. Li, *Commun. Chem.* **2022**, *5*, 1–16.
[15] M. Inukai, F. Isono, A. Takatsuki, *Antimicrob. Agents Chemother.* **1993**, *37*, 980–983.
[16] P. E. Brandish, K. I. Kimura, M. Inukai, R. Southgate, J. T. Lonsdale, T. D. H. Bugg, *Antimicrob. Agents Chemother.* **1996**, *40*, 1640–1644.
[17] D. Wiegmann, S. Koppermann, M. Wirth, G. Niro, K. Leyerer, C. Ducho, *Beilstein J. Org. Chem.* **2016**, *12*, 769–795.
[18] Z. Cui, X. Wang, X. Liu, A. Lemke, S. Koppermann, C. Ducho, J. Rohr, J. S. Thorson, S. G. Van Lanen, *Antimicrob. Agents Chemother.* **2018**, *62*, e00193–18.
[19] A. D. Elbein, *Annu. Rev. Biochem.* **1987**, *56*, 497–534.
[20] A. Takatsukki, K. Kawamura, M. Okina, Y. Kodama, T. Ito, G. Tamura, *Agric. Biol. Chem.* **1977**, *41*, 2307–2309.
[21] T. Ito, Y. Kodama, K. Kawamura, K. Suzuki, A. Takatsuki, G. Tamura, *Agric. Biol. Chem.* **1977**, *41*, 2303–2305.
[22] B. C. Chung, J. Zhao, R. A. Gillespie, D. Y. Kwon, Z. Guan, J. Hong, P. Zhou, S. Y. Lee, *Science.* **2013**, *341*, 1012–1016.
[23] A. Karshikoff, *Non-covalent Interactions in Proteins*, Imperial College Press, London, **2006**.
[24] J. Gao, X. Xia, *Science.* **1992**, *258*, 631–635.
[25] A. Warshel, M. Levitt, *J. Mol. Biol.* **1976**, *103*, 227–249.
[26] J. Fanfrlìk, J. Brynda, J. Rezáč, P. Hobza, M. Lepšik, *J. Phys. Chem. B.* **2008**, *112*, 15094–15102.
[27] J. Gao, *Rev. Comput. Chem.* **1995**, *7*, 119–185.
[28] J. Gao, *Acc. Chem. Res.* **1996**, *29*, 298–305.
[29] J. Gao, D. G. Truhlar, *Annu. Rev. Phys. Chem.* **2002**, *53*, 467–505.
[30] C. Hensen, J. C. Hermann, K. Nam, S. Ma, J. Gao, H. D. Höltje, *J. Med. Chem.* **2004**, *47*, 6673–6680.
[31] M. A. Nitsche, M. Ferreria, E. E. Mocskos, M. C. G. Lebrero, *J. Chem. Theory. Comput.* **2014**, *10*, 959–967.
[32] M. J. Field, P. A. Bash, M. Karplus, *J. Comput. Chem.* **1990**, *11*, 700–733.
[33] S. Ahmadi, L. B. Herrera, M. Chehelamirani, J. Hostaš, S. Jalife, D. R. Salahub, *Int. J. Quantum Chem.* **2018**, *118*, 1–34.
[34] A. D. M. Jr, D. Bashford, M. Bellott, R. L. D. Jr, J. D. Evanseck, M. J. Field, S. Fischer, J. Gao, H. Guo, S. Ha, D. Joseph-McCarthy, L. Kuchnir, K. Kuczera, F. T. K. Lau, C. Mattos, S. Michnick, T. Ngo, D. T. Nguyen, B. Prodhom, W. E. Reiher, B. Roux, M. Schlenkrich, J. C. Smith, R. Stote, J. Straub, M. Watanabe, J. Wiórkiewicz-Kuczera, D. Yin, M. Karplus, *J. Phys. Chem. B.* **1998**, *102*, 3586–3616.
[35] W. L. Jorgensen, J. Chandrasekhar, J. D. Madura, R. W. Impey, M. L. Klein, *J. Chem. Phys.* **1983**, *79*, 926–935.
[36] R. F. W. Bader, C. Cheng, *J. Phys. Chem.* **1989**, *93*, 2946–2956.
[37] R. F. W. Bader, *Atoms in Molecules: A Quantum Theory*, Clarendon Press. Oxford, **1990**.
[38] R. F. W. Bader, *Chem. Rev.* **1991**, *91*, 893–928.
[39] A. E. Reed, L. A. Curtiss, F. Weinhold, *Chem. Rev (Washington, DC, United States).* **1988**, *88*, 899–926.
[40] F. Weinhold, C. R. Landis, *Discovering Chemistry With Natural Bond Orbitals*, John Wiley & Sons, Inc. Wisconsin, **2012**.
[41] S. Malek Zadeh, E. K. Astani, Z. C. Wang, K. Adhikari, R. Rattinam, T. L. Li, *ACS Omega* **2020**, *5*, 22739–22749.
[42] E. K. Astani, S. Malek Zadeh, N. S. Hsu, K. H. Lin, S. Sardari, T. L. Li, *ACS Omega* **2022**, *7*, 32970–32987.
[43] R. B. Best, X. Zhu, J. Shim, P. E. M. Lopes, J. Mittal, M. Feig, A. D. M. Jr, *J. Chem. Theor. Comp.* **2012**, *8*, 3257–3273.
[44] J. V. Ribeiro, R. C. Bernardi, T. Rudack, J. E. Stone, J. C. Phillips, P. L. Freddolino, K. Schulten, *Scientific. Reports.* **2016**, *6*, 1–14.
[45] W. Humphrey, A. Dalke, K. Schulten, *J. Mol. Graph.* **1996**, *14*, 33–38.
[46] M. W. Mahoney, W. L. Jorgensen, *J. Chem. Phys.* **2000**, *112*, 8910–8922.
[47] L. Kalé, R. Skeel, M. Bhandarkar, R. Brunner, A. Gursoy, N. Krawetz, J. Phillips, A. Shinozaki, K. Varadarajan, K. Schulten, *J. Comput. Phys.* **1999**, *151*, 283–312.
[48] J. C. Phillips, R. Braun, W. Wang, J. Gumbart, E. Tajkhorshid, E. Villa, C. Chipot, R. D. Skeel, L. Kalé, K. Schulten, *J. Comput. Chem.* **2005**, *26*, 1781–1802.
[49] R. W. Pastor, B. R. Brooks, A. Szabo, *Mol. Phys.* **1988**, *65*, 1409–1419.
[50] D. M. York, T. A. Darden, L. G. Pedersen, *J. Chern. Phys.* **1993**, *99*, 8345–8348.
[51] H. J. Ryckaert, G. Ciccotti, H. J. C. Berendsen, *J. Computat. Phys.* **1977**, *23*, 327–341.
[52] Y. Zhao, D. G. Truhlar, *Theor. Chem. Acc.* **2008**, *120*, 215–241.
[53] Y. Zhao, N. E. Schultz, D. G. Truhlar, *J. Chem. Theory Comput.* **2006**, *2*, 364–382.
[54] R. Li, D. G. Truhlar, *Phys. Chem. Chem. Phys.* **2010**, *12*, 12697–12701.
[55] M. C. R. Melo, R. C. Bernardi, T. Rudack, M. Scheurer, C. Riplinger, J. C. Phillips, J. D. C. Maia, G. B. Rocha, J. V. Ribeiro, J. E. Stone, F. Neese, K. Schulten, Z. L. Schulten, *Nat. Methods.* **2018**, *15*, 351–354.
[56] F. Neese, *WIREs Comput. Mol. Sci.* **2018**, *8*, e1327.
[57] F. Neese, F. Wennmohs, U. Becker, C. Riplinger, *J. Chem. Phys.* **2020**, *152*, 224108.
[58] D. Bakowies, W. Thiel, *J. Phys. Chem. A.* **1996**, *100*, 10580–10594.
[59] A. H. de Vries, P. Sherwood, S. J. Collins, A. M. Rigby, M. Rigutto, G. J. Kramer, *J. Phys. Chem. B.* **1999**, *103*, 6133–6141.
[60] P. Sherwood, A. H. de Vries, S. J. Collins, S. P. Greatbanks, N. A. Burton, M. A. Vincent, I. H. Hillier, *Faraday Discuss.* **1997**, *106*, 79–92.
[61] H. Lin, D. G. Truhlar, *J. Phys. Chem. A.* **2005**, *109*, 3991–4004.
[62] S. J. Grabowski, *Hydrogen Bonding–New Insights*, Springer, **2006**.
[63] S. J. Grabowski, *Chem. Rev.* **2011**, *111*, 2597–2625.
[64] J. C. Slater, *J. Chem. Phys.* **1933**, *1*, 687–691.
[65] R. F. W. Bader, P. M. Beddall, J. P. Jr, *J. Chem. Phys.* **1973**, *58*, 557–566.
[66] R. Bianchi, G. Gervasio, D. Marabello, *Inorg. Chem.* **2000**, *39*, 2360–2366.
[67] C. Gatti, R. Bianchi, R. Destro, F Merati, *THEOCHEM. J. Mol. Struc.* **1992**, *87*, 409–433.
[68] F. B. Konig, J. J. Schonbohm, D. D. Bayles, *J. Comput. Chem.* **2001**, *22*, 545–559.
[69] I. V. Alabugin, M. Manoharan, S. Peabody, F. Weinhold, *J. Am. Chem. Soc.* **2003**, *125*, 5973–5987.
[70] B. Mennucci, E. Cancés, J. Tomasi, *J. Phys. Chem. B.* **1997**, *101*, 10506–10517.
[71] B. Mennucci, J. Tomasi, R. Cammi, J. R. Cheeseman, M. J. Frisch, F. J. Devlin, S. Gabriel, P. J. Stephens, *J. Phys. Chem. A.* **2002**, *106*, 6102–6113.
[72] J. Tomasi, B. Mennucci, R. Cammi, *Chem. Rev.* **2005**, *105*, 2999–3093.
[73] M. Karplus, G. A. Petsko, *Nature.* **1990**, *347*, 631–639.
[74] C. D. Snow, H. Nguyen, V. S. Pande, M. Gruebele, *Nature.* **2002**, *420*, 102–108.
[75] B. N. Dominy, C. L. Brooks, *J. Comput. Chem.* **2002**, *23*, 147–160.
[76] F. Jensen, *Introduction to Computational Chemistry*, John Wiley & Sons, Ltd. Chichester West Sussex, **2017**.
[77] U. Koch, P. L. A. Popelier, *J. Phys. Chem. A.* **1995**, *99*, 9747–9754.
[78] E. Espinosa, E. Molins, C. Lecomte, *Chem. Phys. Lett.* **1998**, *285*, 170–173.
[79] E. Espinosa, I. Alkorta, I. Rozas, J. Elguero, E. Molins, *Chem. Phys. Lett.* **2001**, *336*, 457–461.
[80] E. Espinosa, I. Alkorta, J. Elguero, E. Molins, *J. Chem. Phys.* **2002**, *117*, 5529–5542.
[81] G. A. Jeffrey, W. Saenger, *Hydrogen Bonding in Biology and Chemistry*, Springer-Verlag. Berlin, **1991**.
[82] G. A. Jeffrey, *An Introduction to Hydrogen Bonding*, Oxford University Press. New York, **1997**.
[83] G. R. Desiraju, T. Steiner, *The Weak Hydrogen Bond in Structural Chemistry and Biology*, Oxford University Press. Oxford, **1999**.
[84] S. Scheiner, *Hydrogen Bonding. A Theoretical Perspective*, Oxford University Press. Oxford, **1997**.
[85] T. Steiner, *Angew. Chem. Int. Ed.* **2002**, *41*, 48–76.
[86] G. R. Desiraju, *Acc. Chem. Res.* **2002**, *35*, 565–573.
[87] I. Rozas, I. Alkorta, J. Elguero, *J. Am. Chem. Soc.* **2000**, *122*, 11154–11161.
[88] Y. Y. Dong, H. Wang, A. C. W. Pike, S. A. Cochrane, S. Hamedzadeh, F. J. Wyszyński, S. R. Bushell, S. F. Royer, D. A. Widdick, A. Sajid, H. I. Boshoff, Y. Park, R. Lucas, W. M. Liu, S. S. Lee, T. Machida, L. Minall, S. Mehmood, K. Belaya, W. W. Liu, A. Chu, L. Shrestha, S. M. M. Mukhopadhyay, C. S. Damerell, R. Chalk, N. A. Burgess-Brown, M. J. Bibb, C. E. Barry III, C. V. Robinson, D. Beeson, B. G. Davis, E. P. Carpenter, *Cell.* **2018**, *175*, 1045–1058.
[89] E. Astani, E. Heshmati, C. J. Chen, N. L. Hadipour, S. Shekarsaraei, *Chem. Phys. Lett.* **2016**, *653*, 78–84.
[90] E. K. Astani, N. L. Hadipour, C. J. Chen, *Chem. Phys. Lett.* **2017**, *672*, 80–88.
[91] E. K. Astani, N. C. Chen, Y. C. Huang, A. Bahrami, L. Y. Chen, P. R. Lin, H. H. Guana, C. C. Lina, P. Chuankhayana, N. L. Hadipour, C. J. Chen, *J. Mol. Graph. Model.* **2017**, *78*, 61–73.
[92] E. K. Astani, N. C. Chen, Y. C. Huang, S. Ersali, P. J. Lin, H. H. Guan, C. C. Lin, P. Chuankhayan, C. J. Chen, *ACS Omega* **2020**, *5*, 3428–3443.
[93] S. F. Boys, F. Bernardi, *Mol. Phys.* **1970**, *19*, 553–566.

Manuscript received: July 6, 2023